Article

Thalamocortical transcriptional gates coordinate memory stabilization

https://doi.org/10.1038/s41586-025-09774-6

Received: 26 September 2024

Accepted: 17 October 2025

Published online: 26 November 2025

Check for updates

Andrea Terceros[1,5], Celine Chen[1,5], Yujin Harada[1], Tim Eilers[1], Millennium Gebremedhin[1], Pierre-Jacques Hamard[2], Richard Koche[2], Roshan Sharma[3,4] & Priya Rajasethupathy[1]✉

The molecular mechanisms that enable memories to persist over long timescales from days to weeks and months are still poorly understood[1]. Here, to develop insights into this process, we created a behavioural task in which mice formed multiple memories but only consolidated some, while forgetting others, over the span of weeks. We then monitored circuit-specific molecular programs that diverged between consolidated and forgotten memories. We identified multiple distinct waves of transcription, that is, cellular macrostates, in the thalamocortical circuit that defined memory persistence. Of note, a small set of transcriptional regulators orchestrated broad molecular programs that enabled entry into these macrostates. Targeted CRISPR-knockout studies revealed that although these transcriptional regulators had no effects on memory formation, they had prominent, causal and strikingly time-dependent roles in memory stabilization. In particular, the calmodulin-dependent transcription factor CAMTA1 was required for initial memory maintenance over days, whereas the transcription factor TCF4 and the histone methyltransferase ASH1L were required later to maintain memory over weeks. These results identify a critical CAMTA1–TCF4–ASH1L thalamocortical transcriptional cascade that is required for memory stabilization and put forth a model in which the sequential recruitment of circuit-specific transcriptional programs enables memory maintenance over progressively longer timescales.

Memories are maintained across vastly different timescales, from hours to days, months and years. The molecular mechanisms by which memories are stabilized over progressively longer timescales are still poorly understood. A key insight came from early observations that transcriptional blockers, although leaving short-term memories intact, prevented the formation of longer-term memories, in animals from honeybees to goldfish to mice[2–5]. These and other studies revealed that the synthesis of new proteins is required to prolong hour-long memories to days-long memories[6]. One transcription factor, CREB1, has been implicated in this process, as its suppression prevents long-term memory formation[7–11], whereas its activation can potentiate the conversion of a transient memory into an overnight memory[12–16]. Thus, the role of transcription in sensing transient signals and activating genes that can prolong functional and structural changes at synapses provides a framework for extending memory from hours to days (synaptic consolidation)[17–19]. However, the molecular programs recruited in extended brain circuits that enable memories to persist on longer timescales, over weeks, months or even a lifetime (systems consolidation), are as yet unknown.

Previous work has detailed that memories can be stabilized through a process of consolidation and reconsolidation[20–22], suggesting that additional transcriptional programs may be recruited to extend memories over longer timescales. Furthermore, epigenetic factors have important roles in maintaining cellular memory[23,24], for instance as cell lineages are specified and maintained during development. Finally, local protein synthesis and long-lived enzymatic and structural changes may also work together to extend memory persistence[25,26]. To bridge these models and to gain insights into the longer-timescale maintenance of memories, we developed a behavioural task in which some memories are consolidated, whereas others are forgotten over the span of weeks. We then developed approaches to study evolving cellular transcriptomes that are a signature of consolidated memories, followed by loss-of-function gene manipulations and assessment of their effects on memory maintenance. We identified discrete waves of transcription in the thalamocortical circuit, governed by specific, non-canonical, memory-related transcriptional regulators, that are required for the progressive stabilization of memories over long timescales.

A behavioural task to monitor memory persistence

To identify molecular programs associated with memory persistence, we began by developing a behavioural task in which mice form multiple memories but only consolidate some, while forgetting others over the span of weeks. Because repetition during learning influence memory persistence, we trained mice to learn context–outcome associations that were presented at varying frequencies. Thus, mice were

[1]Laboratory of Neural Dynamics and Cognition, The Rockefeller University, New York, NY, USA. [2]Epigenetics Research Innovation Lab, Memorial Sloan Kettering Cancer Center, New York, NY, USA. [3]Single-Cell Analytics Innovation Lab, Memorial Sloan Kettering Cancer Center, New York, NY, USA. [4]Computational and Systems Biology Program, Memorial Sloan Kettering Cancer Center, New York, NY, USA. [5]These authors contributed equally: Andrea Terceros, Celine Chen. ✉e-mail: priya@rockefeller.edu

presented with two reward-associated contexts, one at high repetition (HR; approximately 50% of trials) and the other at low repetition (LR; approximately 22% of trials), with the expectation that mice would learn both contexts but maintain memory of only the HR context (by licking in anticipation of reward). To avoid continuous non-associative licking, we randomly interleaved the two reward contexts with an aversive context (approximately 28%) for a total of about 50 trials per session, over a 7-day learning period (Fig. 1a, top). To control the frequency of context presentations and record behaviours at high temporal precision, while maximizing the number of trials, we implemented this behaviour as a head-fixed virtual-reality-based task.

In brief, mice navigated on an axially fixed track ball in a virtual reality environment composed of a corridor with three distinct zones: start, cue and outcome zone. Trials were initiated in the start zone. Then, mice entered one of three cue zones, two of which were paired to a water reward in the outcome zone (HR and LR), whereas the other was paired to an aversive air puff (Fig. 1a, bottom). The cues for each context were designed to be multi-modal (visual, auditory and olfactory) and spatial in nature to ensure hippocampal dependency during memory formation. By the end of training, mice reliably learned the context associations by exhibiting anticipatory licking in the two contexts that predicted reward while suppressing licking in the context that predicted an aversive air puff (Fig. 1b, top). During the retrieval phase, mice were presented with probe trials at a recent (day 1) and remote (day 21) timepoint, and lick rates in the outcome zone provided a measure of recall in the absence of reinforcement. Mice demonstrated successful recall of both the HR and the LR contexts at the recent time, as evidenced by notable differences in raw lick rates in outcome zones and by high lick discrimination indices (Fig. 1b, bottom, and 1c). Over time, mice preferentially maintained memory of the HR context, while failing to recall the LR context (Fig. 1c, $P < 0.001$ between recent and remote for LR, paired two-tailed *t*-test with Bonferroni–Dunn correction). These differential lick rates did not exist when cue–outcome pairs were shuffled (Extended Data Fig. 1a), ensuring that mice did not display intrinsic lick preferences for one context over another, but rather formed learned associations.

Although the formation of contextual memories initially requires the hippocampus (HPC), the subsequent days-to-weeks-long consolidation process becomes increasingly dependent on cortical structures, particularly the anterior cingulate region (ACC) of the prefrontal cortex[27]. We conducted optogenetic loss-of-function experiments to test the hippocampal and cortical dependency of memory in this task. We expressed the inhibitory opsin soma-targeted Guillardia theta anion channelrhodopsin-2 (stGtACR2) bilaterally in either the HPC (CA1 region) or the anterior cingulate cortex (layers 2/3) and delivered light in the cue zones to silence these regions during recent or remote retrieval. As expected, inhibition of the HPC during retrieval led to a near-complete deficit in recent memory recall, whereas inhibition of the ACC resulted in intact recent memory but a strong remote memory deficit (Extended Data Fig. 1b,c).

We previously demonstrated that the anterior thalamus (ANT) is an important conduit that supports hippocampal-to-cortical memory consolidation[28]. We thus tested whether the ANT-to-ACC projection is required for memory consolidation in this new task, and we surveyed the relative contributions of other known ACC-projecting pathways to memory consolidation. We expressed AAVretro-Cre in the ACC and synthetic-intron optimized (SIO)-stGtACR2–mCherry (or Floxed–mCherry control) bilaterally in the ANT, retrosplenial cortex (RSC), basolateral amygdala (BLA) or entorhinal cortex (EC) in separate cohorts of mice. We then performed projection-specific silencing of each of these pathways during training and tested the effects on recent and remote recall (Fig. 1d). We also included cohorts of mice expressing local, bilateral stGtACR2 in the HPC or ACC for comparison. We observed that although some manipulations produced strong deficits in memory formation (HPC, EC→ACC), others produced no deficits in memory formation or consolidation (RSC→ACC, BLA→ACC, local ACC; Fig. 1e, representative raw lick traces in Fig. 1f and Extended Data Fig. 1d). Of note, only the ANT→ACC manipulation left learning and recent memory intact but produced an isolated deficit in remote memory consolidation. This effect size was particularly striking, with fully intact recent recall (discrimination index of approximately 0.7), comparable to controls, but a near-complete deficit in remote recall (discrimination index of approximately 0.1; Fig. 1e; $P = 0.0057$ for recent versus remote, paired two-tailed *t*-test with Bonferroni–Dunn correction). These results support a prominent role for the HPC–ANT–ACC pathway in memory consolidation.

In addition, we tested whether activation of the ANT→ACC circuit during training would be sufficient to improve recall of LR at the remote time (which we have previously found to be true[28] in a different behavioural task). We expressed the stabilized step-function opsin in the ANT→ACC projection and delivered light only during training. Although this manipulation had no effect on learning, it significantly enhanced the LR memory at remote time, which would have otherwise been forgotten (Fig. 1g,h; $P = 0.00048$, paired two-tailed *t*-test with Bonferroni–Dunn correction). We thus established a behavioural task and its neural circuit dependencies, which allowed us to study the diverging molecular programs associated with memory persistence.

Distinct thalamic and cortical programs associated with memory maintenance

Although molecular programs in the HPC that stabilize overnight memories have been well studied, relatively little is understood about molecular programs that extend memories from days into weeks. Given the requirement of the ANT–ACC circuit in supporting days-to-weeks-long memories, we next studied how molecular programs in this circuit diverge between HR (eventually consolidated memories) and LR (eventually forgotten memories) over time. We reasoned that the process of memory consolidation may drive some neurons into cellular states that are unique to the HR condition. To test this, we performed single-cell RNA sequencing in the ANT–ACC circuit at repeated time points to capture the evolving molecular processes at cellular resolution.

We trained a cohort of 48 mice on our behavioural task. All mice were exposed to the same three contexts (HR, LR and aversive) during the training block and were split into cohorts that recalled either HR or LR contexts during retrieval. Independent mice were used for each context (HR or LR) and time point (training early or late; retrieval recent, mid or remote), resulting in at least $n = 3$ mice per condition for library preparation and single-cell sequencing (Fig. 2a). As before, mice learned the HR and LR context associations equally well but exhibited strong divergence in behavioural recall at remote retrieval (Extended Data Fig. 2a–c). We merged all cells from all conditions, and after standard preprocessing, clustered all cells and visualized the data using a uniform manifold approximation and projection (UMAP) embedding (Fig. 2b and Extended Data Fig. 2d–i,m,n). The resulting clusters were annotated into major cell types[29,30] (Supplementary Tables 1 and 2 and Supplementary Fig. 2a). Sub-clustering of the ANT and ACC neurons (Fig. 2c,e) demarcated excitatory from inhibitory neuronal classes (Extended Data Fig. 2j,k,o). On the basis of the average expression of marker genes, we assigned cells to anterior versus posterior nuclei in the ANT (Fig. 2d) and delineated the distinct cortical layers in the ACC (Fig. 2f and Extended Data Fig. 2p,q). Batch effects were negligible, as similar representations of neuronal classes were observed regardless of sample collection day (Extended Data Fig. 2l,r).

To determine whether the transcriptomic profiles of neurons associated with HR versus LR diverge over time, we identified differentially expressed genes (DEGs) at each time point (Fig. 2g,i and Supplementary Table 3). We used the DEGs to measure the transcriptomic distance between the earliest collected time point and each successive time point[31]. We found that the transcriptional divergence between

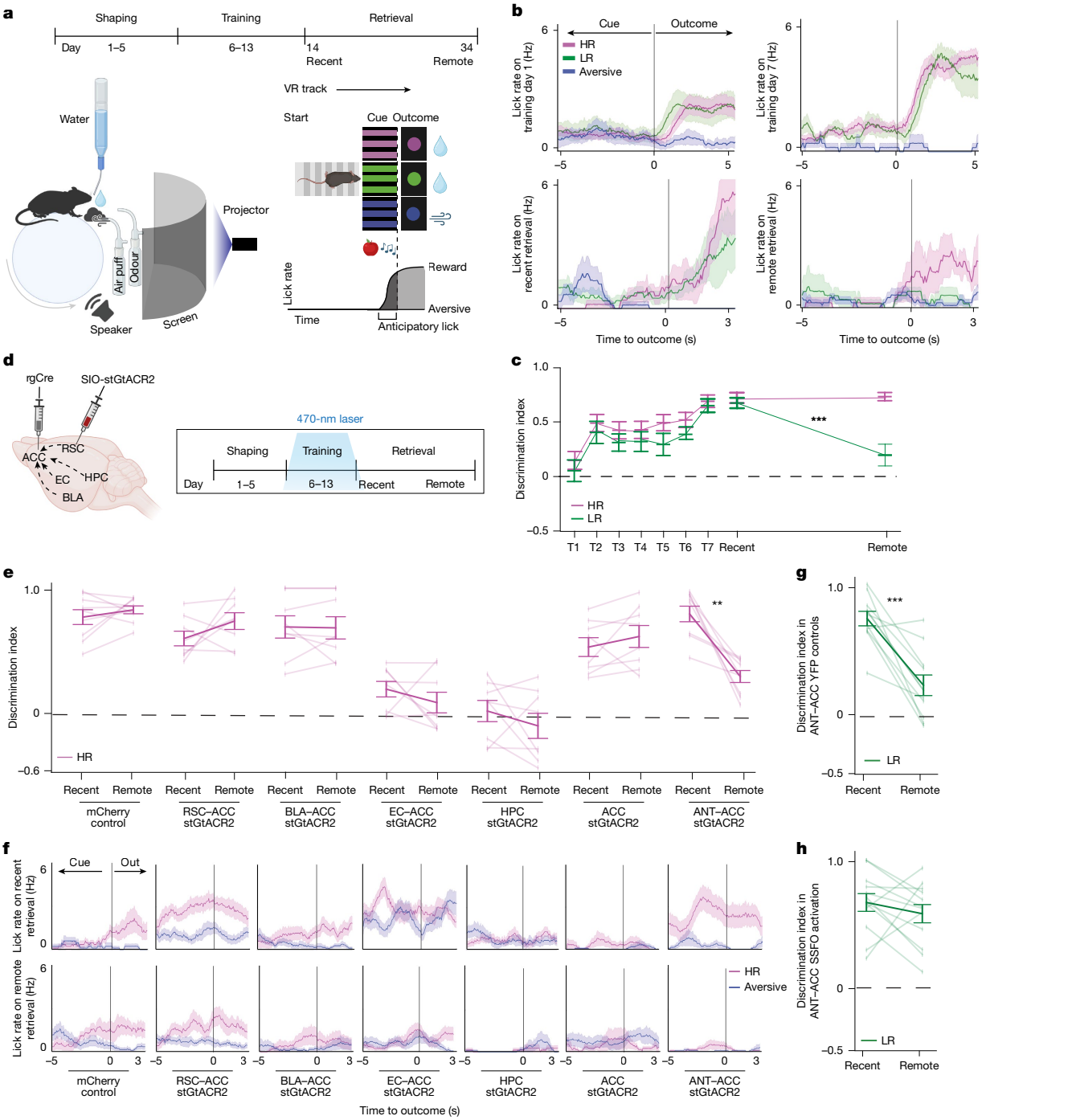

Fig. 1 | A behavioural task to monitor memory persistence requires the HPC, ANT and ACC. a, Top, timeline of the behavioural task from shaping (days 1–5), through training (days 6–13) and retrieval (days 14 and 34). Bottom left, schematic of the virtual reality (VR) experimental setup. Bottom right, the virtual reality linear track with start, cue and outcome zones, and example lick rate. **b**, Representative lick traces from one mouse per cohort showing trial averages on the first and last days of training (top), and recent and remote retrieval (bottom); no reinforcement was given in the outcome zone during retrieval; n = approximately 50 trials per session. Data are mean ± s.e.m. **c**, Quantification of discrimination indices (DIs) of learning and retrieval in HR and LR (n = 24 mice); dashed line, DI = 0 (chance). Data are mean ± s.e.m. ***P = 0.000062 between recent and remote retrieval for LR. **d**, Injection strategy to target projections to the ACC from the ANT, retrosplenial cortex (RSC), entorhinal cortex (EC) and basolateral amygdala (BLA) in SIO-stGtACR2 opsin cohorts (left). Local stGtACR2 was injected in the HPC and ACC. Light was delivered during cue periods of training sessions only, and memory was tested on recent and remote time points (right). **e**, Quantification of discrimination indices between HR and aversive lick rates; dashed line, DI = 0 (chance). n = 9 control mCherry mice and n = 9 mice for the ANT→ACC inhibition cohort (SIO-stGtACR2); n = 8 mice each for the RSC→ACC, BLA→ACC, EC→ACC, local HPC and local ACC inhibition cohorts (SIO-stGtACR2 or stGtACR2). Data are trial-averaged performances of individual mice (faded lines) and mean (solid line) ± s.e.m. **P = 0.0057 for ANT→ACC SIO-stGtACR2. **f**, Representative raw lick traces from one mouse for each cohort in panel **e** (n = 30–40 trials). Data are mean ± s.e.m. **g**, Quantification of DIs (LR versus aversive) of YFP no opsin controls at recent and remote retrieval (n = 10 mice). Dashed line, DI = 0 (chance). Data are trial-averaged performances of individual mice (faded lines) and mean (solid line) ± s.e.m. ***P = 0.00048. **h**, As in **g**, but for ANT→ACC stabilized step-function opsin (SSFO) activation (n = 12 mice). **c**,**e**,**g**,**h**, Paired two-tailed Student's t-test with Bonferroni–Dunn correction. rgCre, retrograde Cre. The schematics in panels **a**,**d** were created using BioRender (https://biorender.com).

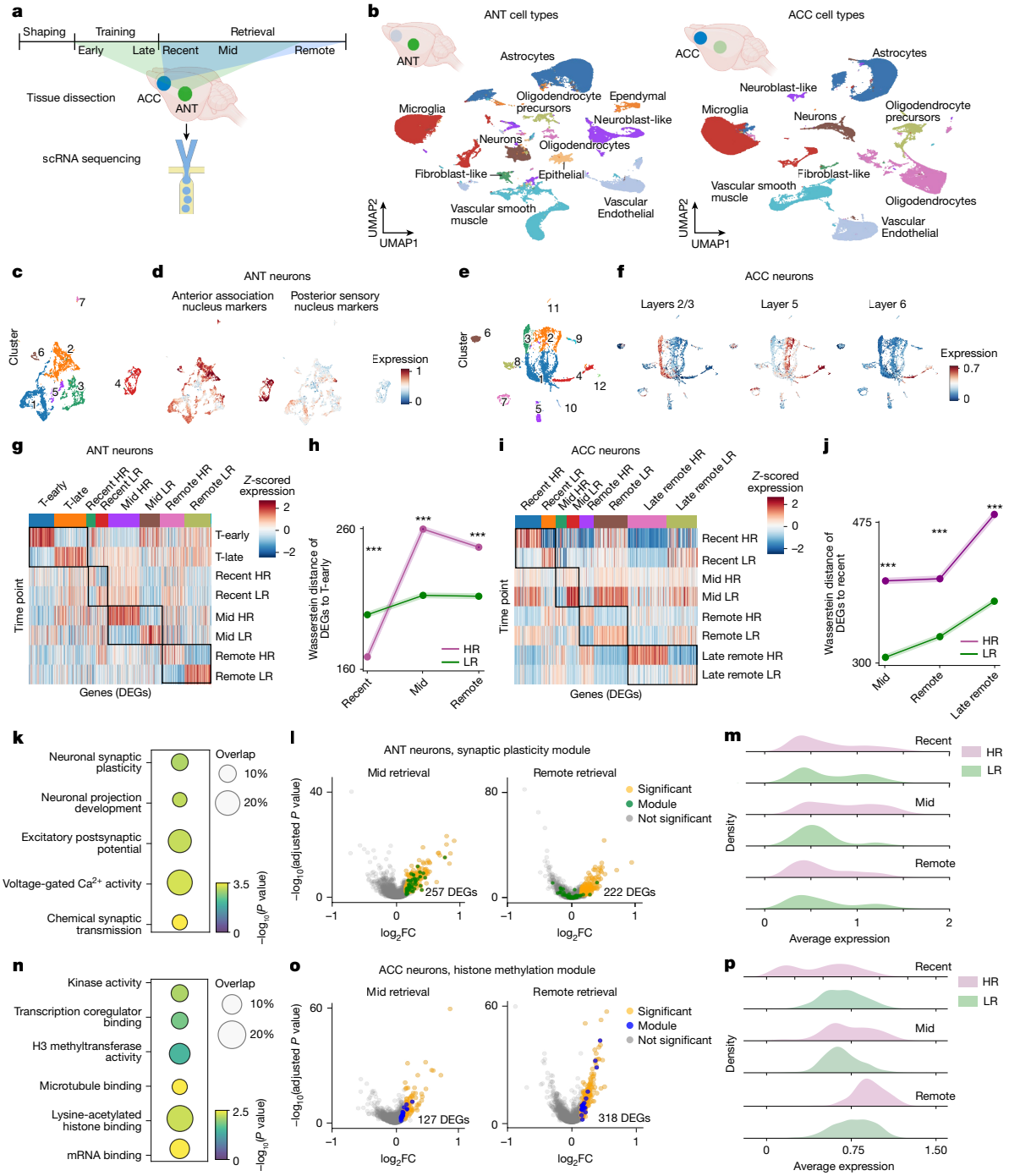

Fig. 2 | Distinct transcriptional programs are activated in the ANT and ACC during memory stabilization. a, Schematic representation of the single-cell RNA (scRNA) sequencing workflow. **b**, UMAP visualization of all cell types collected from the ANT (n = 176,566 cells from n = 23 mice; left) and UMAP of all cell types collected from the ACC (n = 145,327 cells from n = 24 mice; right), clustered on the basis of expression of canonical markers. **c**,**e**, UMAP sub-clustering of cells identified as ANT neurons (**c**; n = 5,535 neurons) or ACC neurons (**e**; n = 5,671 neurons), coloured by cluster number. **d**,**f**, Expression of marker genes of anterior or posterior thalamic nuclei in ANT neurons (**d**) or cortical layers in ACC neurons (**f**). Units are $\log_2$ counts per million (CPM) + 1. **g**,**i**, Heatmap of Z-scored expression of DEGs in each condition in the ANT (**g**) or the ACC (**i**) across time points. Columns are DEGs, and rows are time points. n = 53–164 DEGs per time point (units are $\log_2$CPM + 1). **h**,**j**, Wasserstein distances of DEGs between HR or LR to early training in the ANT (**h**) and to recent retrieval in the ACC (**j**). ***P < 0.0001 at recent, mid and remote retrieval HR versus LR in the ANT; ***P < 0.0001 at mid, remote and late remote retrieval HR versus LR in the ACC; one-way ANOVA with Bonferroni correction. **k**,**n**, Gene Ontology (GO) analysis of DEGs in HR mid-retrieval in ANT (**k**) or ACC (**n**) neurons. GO enrichment was performed using the one-tailed hypergeometric test (over-representation analysis), with multiple comparisons correction. The colour gradient represents the nominal $-\log_{10}$(P value), and the circle size indicates the percentage of genes within a GO term overlapping with total DEGs. **l**,**o**, Volcano plots of DEGs between HR versus LR at mid (left) and remote (right) retrieval in ANT neurons (**l**), and mid (left) and late remote (right) retrieval in the ACC (**o**). Labelled dots represent genes contributing to synaptic plasticity (green, **l**) or histone methylation (blue, **o**) GO modules. Cut-off P < 0.05, cut-off $\log_2$ fold change (FC) ≥ 0.015; P values adjusted for multiple comparisons using the Benjamini–Hochberg method. DEGs were determined through a two-part generalized linear hurdle model. **m**,**p**, Ridge plots of average expression of a plasticity GO module in the ANT (**m**) or histone methylation in the ACC (**p**) across retrieval days in HR (purple) or LR (green) neurons (n = 18–25 genes per module). The y axis represents the density of neuronal population. The schematics in panels **a**,**b** were created using BioRender (https://biorender.com). T-early, early training; T-late, late training.

HR and LR begins as early as recent recall, far preceding behavioural divergence. Although divergence in the ANT attenuates by remote retrieval, the ACC exhibits sustained transcriptional separation through the late-remote time point (Fig. 2h,j). Similar transcriptional divergences were observed when using all genes, suggesting that a subset of DEGs may drive the observed global divergence, and no divergence was observed when using a random subset of genes of similar size to the DEGs (Extended Data Fig. 3a). Gene Ontology pathway analysis of HR DEGs revealed enrichment of synaptic plasticity modules in the ANT, whereas histone methylation modules were enriched in the ACC (Fig. 2k,n and Extended Data Fig. 3b–d). Of note, the plasticity-related programs in the ANT peaked transiently at mid-retrieval and decreased in expression by remote retrieval, whereas the chromatin-related modules in the ACC exhibited sustained expression into remote time points (Fig. 2l,m,o,p and Extended Data Fig. 3e).

To assess whether specific cell types contribute disproportionately to the DEGs between HR and LR, we examined HR versus LR DEGs across cell types and found that DEGs derived from the dominant neuron class in ANT and ACC (*Vglut2*$^+$ and *Vglut1*$^+$, respectively) closely mirrored DEGs derived from the overall population (Extended Data Fig. 3f,g). We additionally classified ACC neurons by cortical layer identity and found that DEGs from cortical layers 2/3 and 6 exhibited upregulation of histone methyltransferase-related pathways at the remote time point. This suggests that chromatin remodelling changes in the ACC may be restricted to certain cortical layers, where changes in layer 6 corticothalamic long-range plasticity may contribute to the layer 2/3 within-region stabilization of corticocortical connections (Extended Data Fig. 3h).

Together, these results reveal that the ANT and ACC engage distinct transcriptional programs—synaptic plasticity pathways in the ANT and chromatin-regulatory pathways in the ACC—that persist to varying degrees throughout memory consolidation.

Key transcriptional regulators coordinate cellular macrostates and memory persistence

We hypothesized that transcriptional divergence between HR and LR reflects occupancy of a phenotypic continuum, rather than of discrete states. Thus, to gain insight into the temporal dynamics of possible phenotypic shifts in the ANT and ACC, we performed pseudotime trajectory analysis on neurons from both regions collected from mice performing the behavioural task above. In brief, we applied the Palantir algorithm[32] to order cells along a continuum on the basis of phenotypic similarity. Pseudotime trajectory analyses have been traditionally used to map cell-state transitions in developmental and cancer studies. Here we used Palantir to capture the temporal progression of cellular states associated with memory persistence.

The start of the pseudotime trajectory was defined by a random cell from the earliest time point (early training in the ANT), and the remaining cells were aligned along a pseudotime continuum on the basis of phenotypic similarity. In the ANT, Palantir identified two apex branches representing distinct extreme phenotypic macrostates (Fig. 3a). We next overlaid cells from the HR and LR conditions and found atypical distribution of cells from each time point. During training and recent retrieval, both HR and LR neurons occupied areas closer to the pseudotime origin. By contrast, during mid and remote retrieval, only HR neurons diverged along the trajectory reaching unique macrostates (we term these states 'early' and 'late' consolidation; Fig. 3b,c). Thus, HR neurons attain unique phenotypic states during memory stabilization, which may define memory persistence.

Of note, the observed early-consolidation and late-consolidation cellular macrostates were not simply batch effects related to sample collection or driven by the performance of a single mouse (Extended Data Fig. 4a). Moreover, shifts between the HR and LR conditions along the trajectory do not represent merely the passage of time, but rather evolving cell states, as not all ANT HR cells reached the early-consolidation or late-consolidation macrostates (a comparable proportion to the approximately 20% of cells that encode the HR condition during in vivo imaging in a similar VR task[28]), further underscoring that only a subset of neurons are behaviourally relevant and undergo consolidation-related transcriptomic changes (Fig. 3b, percentages). Relatedly, by mapping *Fos*$^+$ neurons onto the pseudotime (approximately 30% of all neurons per time point in our dataset), we again observed similar HR versus LR trajectory shifts that mirrored the shifts observed for the entire sampled population (Extended Data Fig. 4e,f,h, left).

To further validate the observed shifts in phenotypic states, we confirmed the robustness of our findings using complementary validations. These included: (1) orthogonal trajectory mapping approaches (Extended Data Fig. 5a,b, left, d–g); (2) projection of previously identified gene programs onto our trajectories (Extended Data Fig. 5c); and (3) quantitative PCR from a separate cohort of mice to verify the dynamic changes in gene expression along pseudotime (Extended Data Fig. 6a). These orthogonal approaches confirmed the presence of distinct cellular macrostates associated with memory persistence and upregulation of plasticity-related (at recent time) and structure-related (at remote time) genes.

We repeated the above pseudotime analyses in ACC neurons. In the ACC, Palantir identified one apex macrostate (Fig. 3h). We again overlaid cell densities from HR and LR conditions per time point and found that HR cells progressed further along the pseudotime trajectory (Fig. 3i,j and Extended Data Figs. 4b and 5a,b, right). We noticed that ACC neurons alternated between the 'origin' and the apex branch more than once (Extended Data Fig. 4g,i), suggesting that ACC neurons may undergo dynamic transitions, thus leading to sustained transcriptional activation. Notably, the observed transitions in the ANT and ACC were not driven by heterogeneity in sample collection (Extended Data Fig. 4c,d), nor were they observed in a control cortical region (V1 visual cortex), which is not thought to be involved in contextual memory consolidation (Extended Data Fig. 5i,j).

We next asked what molecular features enable entry into memory-related macrostates in the ANT and ACC. As transcriptional regulators (for example, transcription factors, coactivators or chromatin modifiers) have been previously shown to be key drivers of branch commitment[32,33], we analysed transcriptional regulators (TRs) whose expression changes correlated with early and late branches of the ANT and ACC trajectories (Supplementary Table 4). In the ANT, we considered four transcriptional regulators—all transcription factors—whose expression correlated with early consolidation (CAMTA1 and MYT1L) and late consolidation (MEF2C and TCF4; Fig. 3d). The predicted downstream targets of each of these transcriptional regulators comprised a considerable fraction (approximately 20–30%) of the remote DEGs (Extended Data Fig. 5h, left). In addition, the average expression of predicted targets co-varied with branch state (Fig. 3e,f), thus supporting a role of the transcriptional regulators in gating branch commitment. We verified that these transcriptional regulators are well expressed in the ANT (Extended Data Fig. 6b–d). Subsequent assay for transposase-accessible chromatin using sequencing (ATAC-seq) analysis of ANT neurons (Extended Data Fig. 7a–d) further confirmed increased accessibility of the predicted modules of these transcriptional regulators by mid-retrieval, with varying levels of persistence that mirrored the expression patterns of the transcriptional regulators (Fig. 3g, Extended Data Fig. 7e, left, and Supplementary Fig. 2b). These data identify a set of key transcriptional regulator candidates that appear to orchestrate entry into early-consolidation and late-consolidation macrostates in the ANT.

In the ACC, we identified three transcriptional regulators that defined the late-consolidation macrostate (ASH1L, KMT2A and PRDM2), all of which have a role in histone methylation (Fig. 3k,l,m and Extended Data Fig. 5h, right). Although the *Ash1l*, *Kmt2a* and *Prdm2* ATAC peaks

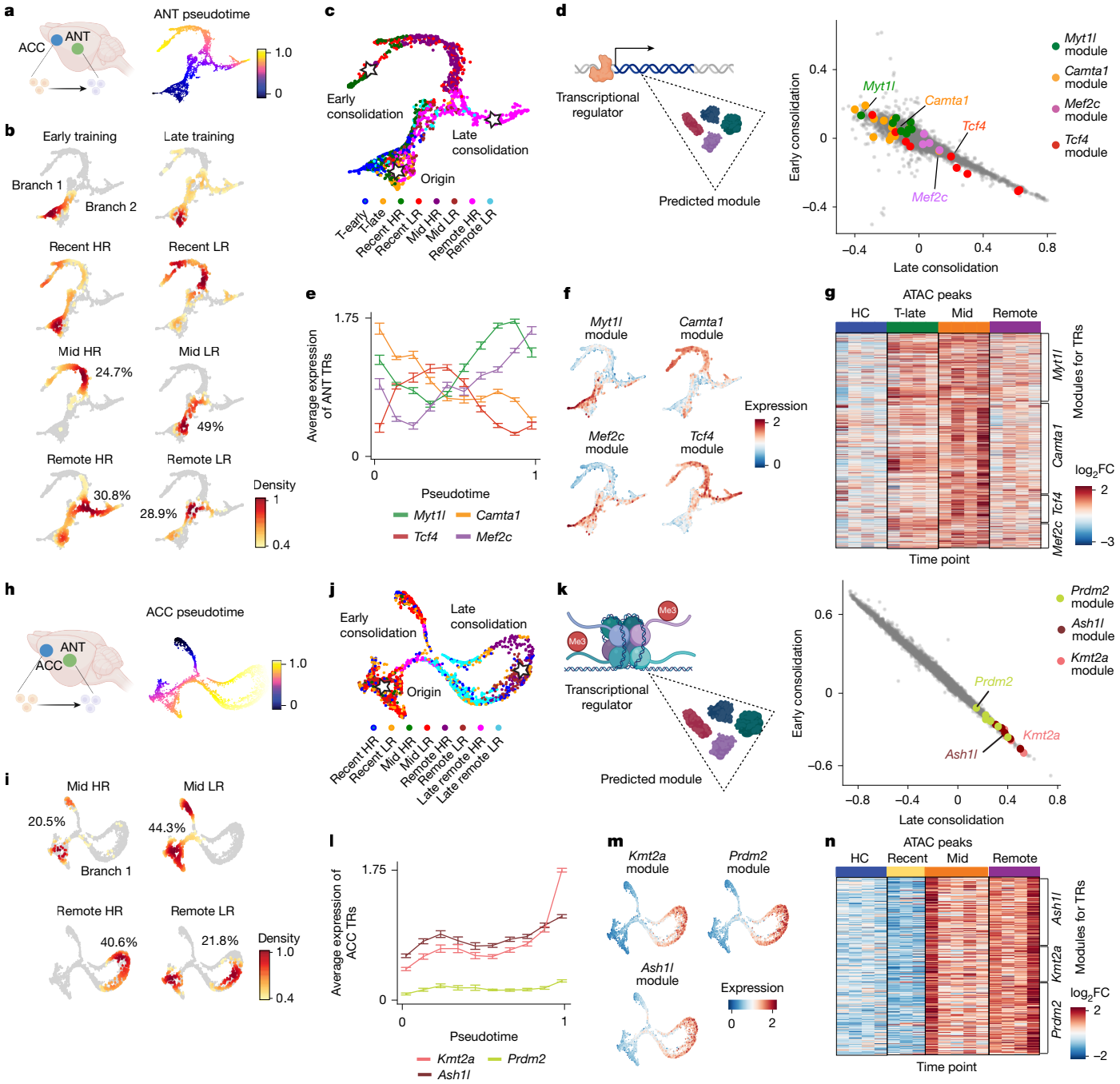

Fig. 3 | Transcriptional regulators define entry into phenotypic states associated with memory persistence. a,**h**, tSNE visualization of ANT (**a**) or ACC (**h**) neurons ordered and coloured by pseudotime. **b**,**i**, Density plots across training and retrieval days of HR and LR ANT (**b**) or ACC (**i**) neurons on the tSNE pseudotime space. The start of the pseudotime is early training in the ANT and recent retrieval in the ACC. The percentages indicate neurons with density ≥0.6. **c**,**j**, Pseudotime tSNE visualization of neurons from the ANT (**c**) or the ACC (**j**) coloured by behavioural time point. The stars highlight 'apex' macrostates inferred by Palantir, which represent the origin of the pseudotime trajectory and early or late consolidation states. **d**,**k**, Left, schematic of predicted modules targeted by transcriptional regulators (TRs) (transcription factors in the ANT (**d**) and histone modifiers in the ACC (**k**)). Right, correlation plots of genes towards the early versus late consolidation macrostate branches for the ANT trajectory (**d**) or the ACC trajectory (**k**). The top correlated TRs with either early or late consolidation states are labelled, as well as representative genes from their predicted target gene modules in matching colours. **e**,**l**, Average expression of ANT or ACC TRs in ANT neurons (**e**) or ACC neurons (**l**) along the ANT or ACC pseudotime trajectory, respectively. Data are mean ± s.e.m., and units are $\log_2$CPM + 1. **f**,**m**, tSNE visualizations of expression levels of the predicted target gene modules for ANT (**f**) or ACC (**m**) TRs. $n = 13–46$ genes per module. **g**,**n**, *Z*-scored accessibility of ATAC peaks of modules for ANT (**g**) or ACC (**n**) predicted TRs across time points. The columns are biological replicates ($n = 3–5$ mice per time point), and the rows are ATAC peaks for modules for predicted transcriptional regulators. HC, home cage. The schematics in panels **a**,**d**,**h**,**k** were created using BioRender (https://biorender.com).

were most accessible at mid-retrieval (returning to baseline by remote retrieval; Extended Data Fig. 7e, right), the peaks for their predicted modules remained accessible through remote time points (Fig. 3n and Supplementary Fig. 2b). These data reveal sustained expression of chromatin remodelling programs enriched in the ACC in the late phase of consolidation.

Together, these combined pseudotime results indicate that the ANT and ACC neurons may recruit a sparse and distinct set of transcriptional

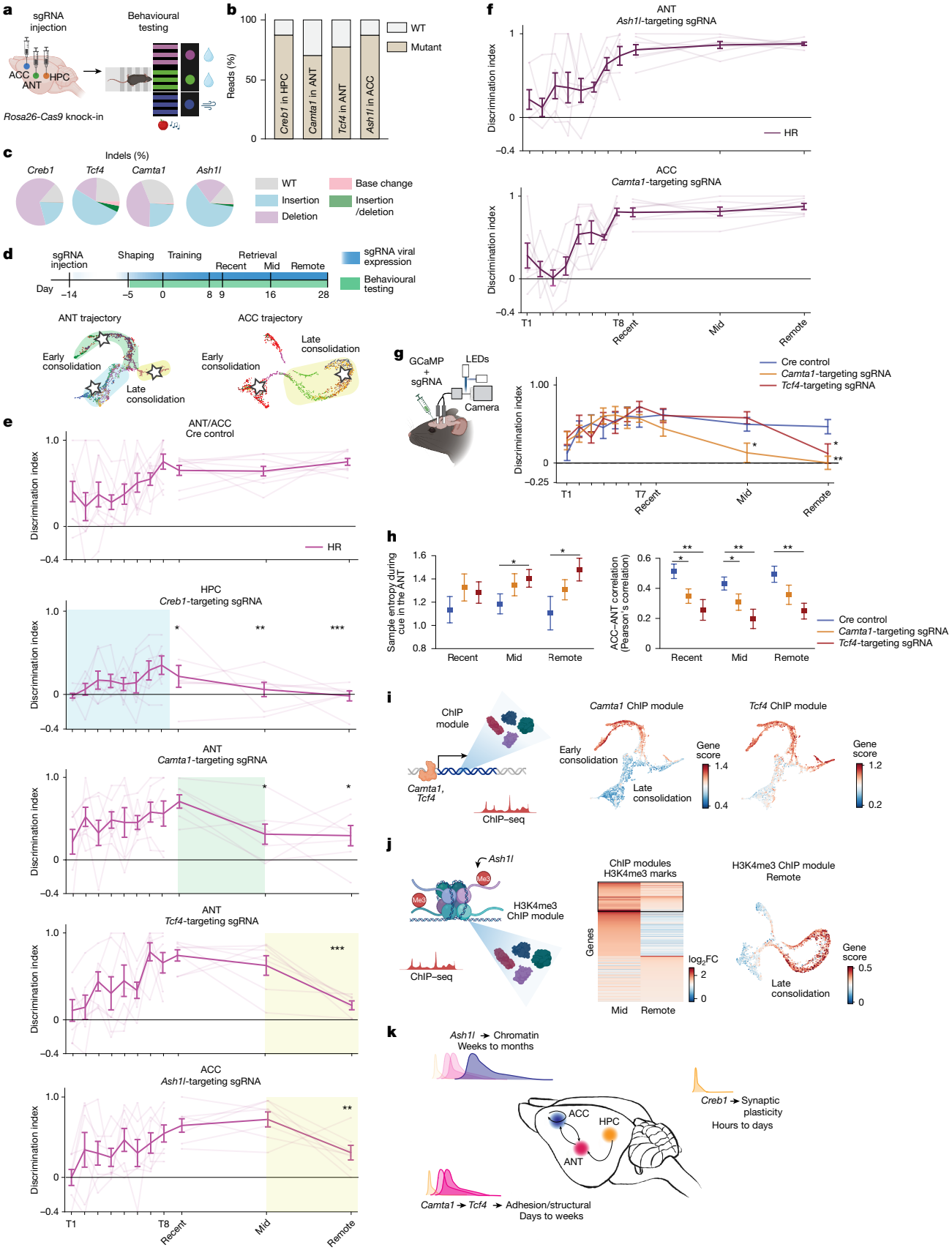

Fig. 4 | See next page for caption.

Fig. 4 | The *Camta1*–*Tcf4*–*Ash1l* thalamocortical transcriptional cascade is required during memory stabilization. a, Schematic of the CRISPR–Cas9 screen workflow. **b**, Percentage of wild type (WT) versus mutant Sanger sequencing reads from genomic DNA isolated from *Rosa26-Cas9* knock-in mice injected with AAV-sgRNA-Cre-GFP. One mouse per gene is shown. **c**, Pie charts illustrating the breakdown of specific insertion or deletion (indel) mutations identified by next-generation sequencing of the PCR amplicon spanning the cut site from mice in panel **b**. For FACS gating strategy for **b**,**c**, refer to Supplementary Fig. 2d. **d**, Timeline of the CRISPR–Cas9 behavioural screen (top), and schematics of ANT (bottom left) and ACC (bottom right) pseudotime trajectories. **e**, Discrimination indices for learning and recall. Control mice expressing AAV-Cre ($n = 8$) were compared with mice expressing AAV-sgRNA-Cre-GFP targeting specific genes in different brain regions: *Creb1* in the HPC ($n = 7$), *Camta1* or *Tcf4* in the ANT ($n = 7$ each) or *Ash1l* in the ACC ($n = 7$). Significant differences versus control are indicated: *Creb1* (*$P = 0.026$ for T8, **$P = 0.0063$ for mid and ***$P = 0.0003$ for remote), *Camta1* (*$P = 0.0288$ for mid and *$P = 0.0466$ for remote), *Tcf4* (***$P = 0.0002$ for remote) and *Ash1l* (**$P = 0.0086$ for remote). The faded lines represent individual mouse performances (trial averaged), and the solid line is the mean; error bars show ± s.e.m. Significance was determined using one-way ANOVA with Bonferroni correction. **f**, Discrimination indices of mice injected with *Ash1l*-targeting sgRNA in the ANT or *Camta1*-targeting sgRNA in the ACC ($n = 7$ mice). Data are trial-averaged performances of individual mice (faded lines) and mean (solid line) ± s.e.m. **g**, Discrimination index of the fibre photometry cohort ($n = 10$ mice per cohort for control and *Tcf4* knockout, and $n = 7$ mice for the *Camta1*-knockout cohort). This cohort was injected and run on behaviour independently from the cohort in **e**. Data are for trial-averaged performances (DIs) across the three cohorts, shown as mean of DIs across all mice ± s.e.m. *$P = 0.0248$ between controls and *Camta1*-targeting sgRNA at mid-retrieval, **$P = 0.0031$ at remote retrieval and *$P = 0.0306$ between controls and *Tcf4*-targeting sgRNA at remote retrieval, using one-way ANOVA with Bonferroni correction. **h**, Sample entropy during cue of HR retrieval sessions in the ANT (left); each point represents a mouse. Data are mean ± s.e.m. *$P = 0.0361$ between controls and *Tcf4*-targeting sgRNA at mid-retrieval and *$P = 0.0221$ at remote retrieval, using unpaired one-tailed Student's *t*-test. Pairwise Pearson's correlations between the ANT and ACC during cue of HR retrieval sessions, at approximately 25 trials per mouse are also shown (right). Each point represents a single mouse. Data are mean ± s.e.m. *$P = 0.0163$ between controls and *Camta1*-targeting sgRNA at recent retrieval and *$P = 0.0464$ at mid-retrieval, **$P = 0.0033$ between controls and *Tcf4*-targeting sgRNA at recent retrieval, and **$P = 0.0036$ at mid-retrieval and **$P = 0.0011$ at remote retrieval, using unpaired one-tailed Student's *t*-test. **i**, Left, schematic depicting transcriptional regulator modules derived from ChIP–seq. The scored average expression of CAMTA1 (middle) or TCF4 ChIP targets overlaid onto the ANT pseudotime trajectory (right) is also shown. **j**, Left, schematic depicting transcriptional regulator modules derived from ChIP–seq. Middle, heatmap of H3K4me3 marks in ACC dissected from WT mice run on the behavioural task, with animals dissected at mid or remote timepoints. Right, the scored average expression of H3K4me3 targets. **k**, Proposed model for the role of CAMTA1, TCF4 and ASH1L in memory stabilization. *Creb1*-dependent early molecular cascades are triggered in the HPC and operate on the scale of hours to days, whereas expression of *Camta1* and *Tcf4* in the ANT extends memories beyond days. In the ACC, histone methylators, such as ASH1L, operate on longer time constants, allowing the stabilization of information across cortical ensembles. The schematics in panels **a**,**g**,**i**,**j** were created using BioRender (https://biorender.com).

regulators, which turn on broad transcriptional programs over different timescales, and that ultimately shape macrostates associated with memory persistence.

A sequential thalamocortical transcriptional cascade is required for memory stabilization

To test whether the identified transcriptional regulators have causal roles in memory stabilization, we performed region-specific knockout of these genes using CRISPR-based in vivo manipulations (Fig. 4a). We tested *Camta1*, *Myt1l*, *Mef2c* and *Tcf4* in the ANT and *Kmt2a* and *Ash1l* in the ACC; we also included *Creb1* in the HPC as a reference. We began by screening many single guide RNAs (sgRNAs) in vitro and selected the most efficient guide for each gene for in vivo behavioural testing (Extended Data Fig. 8a–d and Supplementary Fig. 2c). We delivered an AAV-sgRNA-Cre or control AAV9-Cre into the ANT, ACC or HPC of Rosa26-LSL-spCas9-eGFP mice[34] and catalogued the resulting mutation types (Fig. 4b,c and Supplementary Fig. 2d). We also confirmed knockout at the protein level by immunofluorescence or western blot (Extended Data Fig. 8e–g and Supplementary Fig. 1).

Mice expressed the construct for 2 weeks before starting behavioural testing (Fig. 4d). Control mice successfully learned the task, as demonstrated by a high discrimination indices across time (Fig. 4e, top). As expected, mice with knockout of *Creb1* in the HPC displayed strong learning and early recall deficits (Fig. 4e). Mice expressing sgRNAs targeting the ANT or ACC transcriptional regulators displayed no observable learning deficits. However, knockout of a subset of those transcriptional regulators led to striking and temporally restricted consolidation deficits that were specific to the ANT (early to mid-consolidation) or the ACC (remote consolidation). Knockout of *Camta1* resulted in impaired recall at the intermediate time point, whereas knockout of *Tcf4* produced a recall deficit only at remote time (Fig. 4e; $P = 0.0288$ between controls and *Camta1*-targeting sgRNA at mid-retrieval; $P = 0.0002$ between controls and *Tcf4*-targeting sgRNA at remote retrieval, one-way analysis of variance (ANOVA) with Bonferroni multiple comparison correction). Conversely, knockout of *Myt1l* or *Mef2c* in the ANT resulted in no significant memory impairments (Extended Data Fig. 8h). Of the genes tested in the ACC, only knockout of *Ash1l* resulted in an isolated remote memory deficit (Fig. 4e, bottom; $P = 0.0086$ between controls and *Ash1l*-targeting sgRNA at remote retrieval, one-way ANOVA with Bonferroni multiple comparison correction). Knockout of *Kmt2a* resulted in a trending but not significant remote impairment, which might be explained by redundancy of regulators from the same family (Extended Data Fig. 8h). Of note, the functional effects of CAMTA1 in the ANT and ASH1L in the ACC were region specific, as inverse manipulations, such as knockout of *Camta1* in the ACC or *Ash1l* in the ANT produced no behavioural deficits (Fig. 4f).

To explore the functional contributions of these transcriptional regulators in the ANT–ACC circuit, we performed longitudinal GCaMP-based neural activity recordings in the ANT and ACC during behaviour, comparing controls with *Camta1* or *Tcf4* knockout mice k (Fig. 4g and Extended Data Fig. 9a). We found that the *Camta1* and *Tcf4* knockouts displayed early increases in neural entropy (a measure of neural variability) and significant deficits in ANT-to-ACC functional correlations (Fig. 4h). These initial results suggest that CAMTA1 and TCF4 may coordinate ANT–ACC functional connectivity and plasticity during memory stabilization, and require follow-up investigation.

Finally, to reveal mechanistic insights into the transcriptional targets of CAMTA1, TCF4 and ASH1L and their roles in memory consolidation, we performed chromatin immunoprecipitation followed by sequencing (ChIP–seq) analyses following behaviour along multiple time points (Extended Data Fig. 9b and Supplementary Table 5). We confirmed marked depletion of signal in *Camta1*-knockout and *Tcf4*-knockout cohorts (Extended Data Fig. 9c) and reduced expression of CAMTA1 ChIP-predicted targets by quantitative PCR (Extended Data Fig. 9g). We confirmed that the most strongly depleted peaks in *Camta1*-knockout mice were associated with genes involved in plasticity-related pathways, whereas *Tcf4*-knockout depleted peaks were in genes associated with cell adhesion (Extended Data Fig. 9d–f and Supplementary Fig. 2e). When we overlaid the identified CAMTA1 or TCF4 target genes onto the ANT pseudotime trajectory, we found that the target genes' average expression was enriched primarily along the early-consolidation or late-consolidation branch, respectively (Fig. 4i).

In the ACC, we examined changes in H3K4me3 methylation marks following *Ash1l* knockout, and, although no global changes in H3K4me3 marks were observed (Extended Data Fig. 10a), we found an interesting temporal shift in methylation of gene programs over time: from plasticity-related pathways at mid-retrieval to structural components at remote retrieval (Fig. 4j and Extended Data Fig. 10b,c). *Ash1l* knockout at mid-retrieval resulted in depletion of H3K4me3 methylation marks at promoters of plasticity-associated genes, whereas at remote retrieval, the most depleted peaks occurred on genes involved in structural regulation (Extended Data Fig. 10d–f). Most of the chromatin accessibility of the CAMTA1 gene module derived from our ChIP–seq data returned to baseline levels by the remote time point, with the exception of the TCF4 gene module. By contrast, peaks for the H3K4me3 module in the ACC remained accessible through the remote time point (Extended Data Fig. 10g).

In summary, we identified three transcriptional regulators, CAMTA1, TCF4 and ASH1L, that have sequential, circuit-specific and causal contributions to memory maintenance, providing a mechanism for the continuous stabilization of memory from days to weeks (Fig. 4k).

Discussion

The earliest discovered signalling molecules important for learning and memory were components of the calmodulin–cAMP pathway[35–37]. In addition to these transient mechanisms, the role of protein synthesis and, in particular, the activation of the cAMP-dependent transcription factor CREB1, was found to be important for enabling longer-lasting forms of synaptic plasticity on the order of hours to days. Still, the molecular programs underlying the maintenance of memories on longer timescales have remained elusive. Here we expanded our molecular understanding of memory beyond the well-studied HPC and identify distinct transcriptional regulators, operating initially in the ANT (the calmodulin-sensitive transcription factors CAMTA1 and TCF4), then in the ACC (the histone modifier ASH1L), that propagate memory maintenance progressively from days to weeks. Of note, these transcriptional regulators were not required during learning, but instead had defined, sequential, time-limited roles in memory maintenance. In addition, these effects were circuit specific: CAMTA1 and TCF4 functioned in the ANT and ASH1L in the ACC. Furthermore, we observed little to no effect on memory maintenance when we manipulated other transcriptional regulators, such as MYT1L, MEF2C or KMT2A, whose gene modules also co-varied on similar timescales throughout the behavioural task, further underscoring a critical causal role for CAMTA1, TCF4 and ASH1L in orchestrating progressively longer timescale memory stabilization.

These results thus highlight several important aspects of the memory stabilization process: (1) that beyond the HPC, the thalamocortical circuit has a critical contribution to memory stabilization; (2) that memory stabilization requires the successive recruitment of transcriptional programs operating on progressively longer timescales; and (3) that these time-limited transcriptional programs operate in a circuit-specific manner, providing an explanation for why multiple circuits across the brain are recruited to support continuous memory stabilization. Such a process, operating on multiple timescales, allows for integrating an initial system for fast memory acquisition (but fast decay), with subsequent systems for slower acquisition but longer retention. This not only enables an adaptive trade-off between storage and forgetting[38] but also provides multiple regulatory checkpoints before committing memories to long-term storage (Fig. 4k).

We observed that the ANT and ACC engage shared but also distinct functional pathways to support memory stabilization. In the ANT, CAMTA1 supports synaptic plasticity-related gene expression programs, whereas TCF4 additionally supports structural refinement involving synaptic adhesion and pruning. In the ACC, histone methylation emerges as a critical mechanism for extending memory persistence. It is interesting to note that although ASH1L emerges as a late-phase regulator in the ACC, its targets overlap in function with those of CAMTA1 and TCF4, suggesting a 'priming' mechanism[39,40] to prolong plasticity or structural gene targets necessary for extending synaptic and circuit timescales. Indeed, histone methylation marks tend to persist longer than transcription factor activation, aligning with a model in which the sequential recruitment of transcriptional regulators across the brain enables a progressive reorganization of memories from transiently plastic states to slower, more enduring states. Notably, in human studies, CAMTA1, TCF4 and ASH1L have all been linked to intellectual disability or memory impairment, underscoring their relevance to human cognition[41–43].

These findings support the notion that the basic biological substrates that convert transient stimuli into lasting cellular states—such as those that maintain cell identity[44], immune memory[45] or behavioural state[46]—can be co-opted to support cognitive memories. Indeed, emergent network properties can push transcriptional programs into lasting cellular states that operate on different timescales[47]. Relatedly, epigenetic programs can support even more lasting cellular phenotypes, and pharmacological studies have already highlighted their important roles in the adult brain during learning and memory[48,49]. By identifying specific transcriptional regulators with sequential contributions to memory maintenance, we provide a mechanism for the continuous stabilization of memory over extended timescales.

Online content

Any methods, additional references, Nature Portfolio reporting summaries, source data, extended data, supplementary information, acknowledgements, peer review information; details of author contributions and competing interests; and statements of data and code availability are available at https://doi.org/10.1038/s41586-025-09774-6.

1. Yadav, N., Toader, A. & Rajasethupathy, P. Beyond hippocampus: thalamic and prefrontal contributions to an evolving memory. *Neuron* **112**, 1045–1059 (2024).
2. Agranoff, B. W. & Klinger, P. D. Puromycin effect on memory fixation in the goldfish. *Science* **146**, 952–953 (1964).
3. Flexner, L. B. & Flexner, J. B. Effect of acetoxycycloheximide and of an acetoxycycloheximide-puromycin mixture on cerebral protein synthesis and memory in mice. *Proc. Natl Acad. Sci. USA* **55**, 369–374 (1966).
4. Squire, L. R. & Barondes, S. H. Actinomycin-D: effects on memory at different times after training. *Nature* **225**, 649–650 (1970).
5. Igaz, L. M., Vianna, M. R. M., Medina, J. H. & Izquierdo, I. Two time periods of hippocampal mRNA synthesis are required for memory consolidation of fear-motivated learning. *J. Neurosci.* **22**, 6781–6789 (2002).
6. Kandel, E. R. The molecular biology of memory storage: a dialogue between genes and synapses. *Science* **294**, 1030–1038 (2001).
7. Dash, P. K., Hochner, B. & Kandel, E. R. Injection of the cAMP-responsive element into the nucleus of aplysia sensory neurons blocks long-term facilitation. *Nature* **345**, 718–721 (1990).
8. Alberini, C. M., Ghirardi, M., Metz, R. & Kandel, E. R. C/EBP is an immediate-early gene required for the consolidation of long-term facilitation in aplysia. *Cell* **76**, 1099–1114 (1994).
9. Yin, J. C. et al. Induction of a dominant negative CREB transgene specifically blocks long-term memory in *Drosophila*. *Cell* **79**, 49–58 (1994).
10. Bourtchuladze, R. et al. Deficient long-term memory in mice with a targeted mutation of the cAMP-responsive element-binding protein. *Cell* **79**, 59–68 (1994).
11. Silva, A. J., Kogan, J. H., Frankland, P. W. & Kida, S. CREB and memory. *Annu. Rev. Neurosci.* **21**, 127–148 (1998).
12. Yin, J. C., Del Vecchio, M., Zhou, H. & Tully, T. CREB as a memory modulator: induced expression of a dCREB2 activator isoform enhances long-term memory in *Drosophila*. *Cell* **81**, 107–115 (1995).
13. Bartsch, D., Casadio, A., Karl, K. A., Serodio, P. & Kandel, E. R. CREB1 encodes a nuclear activator, a repressor, and a cytoplasmic modulator that form a regulatory unit critical for long-term facilitation. *Cell* **95**, 211–223 (1998).
14. Josselyn, S. A. et al. Long-term memory is facilitated by cAMP response element-binding protein overexpression in the amygdala. *J. Neurosci.* **21**, 2404–2412 (2001).
15. Barco, A., Alarcon, J. M. & Kandel, E. R. Expression of constitutively active CREB protein facilitates the late phase of long-term potentiation by enhancing synaptic capture. *Cell* **108**, 689–703 (2002).
16. Lin, H.-W., Chen, C.-C., de Belle, J. S., Tully, T. & Chiang, A.-S. CREBA and CREBB in two identified neurons gate long-term memory formation in *Drosophila*. *Proc. Natl Acad. Sci. USA* **118**, e2100624118 (2021).
17. Lamprecht, R. & LeDoux, J. Structural plasticity and memory. *Nat. Rev. Neurosci.* **5**, 45–54 (2004).

18. Carlezon, W. A. Jr, Duman, R. S. & Nestler, E. J. The many faces of CREB. *Trends Neurosci.* **28**, 436–445 (2005).
19. Kandel, E. R. The molecular biology of memory: cAMP, PKA, CRE, CREB-1, CREB-2, and CPEB. *Mol. Brain* **5**, 14 (2012).
20. Nader, K. Memory traces unbound. *Trends Neurosci.* **26**, 65–72 (2003).
21. Alberini, C. M. Mechanisms of memory stabilization: are consolidation and reconsolidation similar or distinct processes? *Trends Neurosci.* **28**, 51–56 (2005).
22. Dudai, Y. Reconsolidation: the advantage of being refocused. *Curr. Opin. Neurobiol.* **16**, 174–178 (2006).
23. Wood, M. A., Hawk, J. D. & Abel, T. Combinatorial chromatin modifications and memory storage: a code for memory? *Learn. Mem.* **13**, 241–244 (2006).
24. Coda, D. M. & Gräff, J. From cellular to fear memory: an epigenetic toolbox to remember. *Curr. Opin. Neurobiol.* **84**, 102829 (2024).
25. Kandel, E. R., Dudai, Y. & Mayford, M. R. The molecular and systems biology of memory. *Cell* **157**, 163–186 (2014).
26. Holt, C. E., Martin, K. C. & Schuman, E. M. Local translation in neurons: visualization and function. *Nat. Struct. Mol. Biol.* **26**, 557–566 (2019).
27. Frankland, P. W. & Bontempi, B. The organization of recent and remote memories. *Nat. Rev. Neurosci.* **6**, 119–130 (2005).
28. Toader, A. C. et al. Anteromedial thalamus gates the selection and stabilization of long-term memories. *Cell* **186**, 1369–1381.e17 (2023).
29. Zeisel, A. et al. Molecular architecture of the mouse nervous system. *Cell* **174**, 999–1014.e22 (2018).
30. Yao, Z. et al. A high-resolution transcriptomic and spatial atlas of cell types in the whole mouse brain. *Nature* **624**, 317–332 (2023).
31. Heumos, L. et al. Pertpy: an end-to-end framework for perturbation analysis. Preprint at *bioRxiv* https://doi.org/10.1101/2024.08.04.606516 (2024).
32. Setty, M. et al. Characterization of cell fate probabilities in single-cell data with Palantir. *Nat. Biotechnol.* **37**, 451–460 (2019).
33. Weiler, P., Lange, M., Klein, M., Pe'er, D. & Theis, F. CellRank 2: unified fate mapping in multiview single-cell data. *Nat. Methods* **21**, 1196–1205 (2024).
34. Platt, R. J. et al. CRISPR-Cas9 knockin mice for genome editing and cancer modeling. *Cell* **159**, 440–455 (2014).
35. Dudai, Y., Jan, Y. N., Byers, D., Quinn, W. G. & Benzer, S. dunce, A mutant of *Drosophila* deficient in learning. *Proc. Natl Acad. Sci. USA* **73**, 1684–1688 (1976).
36. Davis, R. L. Physiology and biochemistry of *Drosophila* learning mutants. *Physiol. Rev.* **76**, 299–317 (1996).
37. Quinn, W. G., Sziber, P. P. & Booker, R. The *Drosophila* memory mutant amnesiac. *Nature* **277**, 212–214 (1979).
38. Fusi, S., Drew, P. J. & Abbott, L. F. Cascade models of synaptically stored memories. *Neuron* **45**, 599–611 (2005).
39. Marco, A. et al. Mapping the epigenomic and transcriptomic interplay during memory formation and recall in the hippocampal engram ensemble. *Nat. Neurosci.* **23**, 1606–1617 (2020).
40. Santoni, G. et al. Chromatin plasticity predetermines neuronal eligibility for memory trace formation. *Science* **385**, eadg9982 (2024).
41. Huentelman, M. J. et al. Calmodulin-binding transcription activator 1 (CAMTA1) alleles predispose human episodic memory performance. *Hum. Mol. Genet.* **16**, 1469–1477 (2007).
42. Teixeira, J. R., Szeto, R. A., Carvalho, V. M. A., Muotri, A. R. & Papes, F. Transcription factor 4 and its association with psychiatric disorders. *Transl. Psychiatry* **11**, 19 (2021).
43. Liu, H. et al. ASH1L mutation caused seizures and intellectual disability in twin sisters. *J. Clin. Neurosci.* **91**, 69–74 (2021).
44. Bintu, L. et al. Dynamics of epigenetic regulation at the single-cell level. *Science* **351**, 720–724 (2016).
45. Larsen, S. B. et al. Establishment, maintenance, and recall of inflammatory memory. *Cell Stem Cell* **28**, 1758–1774.e8 (2021).
46. Stern, S., Kirst, C. & Bargmann, C. I. Neuromodulatory control of long-term behavioral patterns and individuality across development. *Cell* **171**, 1649–1662.e10 (2017).
47. Hergenreder, E. et al. Combined small-molecule treatment accelerates maturation of human pluripotent stem cell-derived neurons. *Nat. Biotechnol.* https://doi.org/10.1038/s41587-023-02031-z (2024).
48. Campbell, R. R. & Wood, M. A. How the epigenome integrates information and reshapes the synapse. *Nat. Rev. Neurosci.* **20**, 133–147 (2019).
49. Mews, P. et al. From circuits to chromatin: the emerging role of epigenetics in mental health. *J. Neurosci.* **41**, 873–882 (2021).

Publisher's note Springer Nature remains neutral with regard to jurisdictional claims in published maps and institutional affiliations.

Springer Nature or its licensor (e.g. a society or other partner) holds exclusive rights to this article under a publishing agreement with the author(s) or other rightsholder(s); author self-archiving of the accepted manuscript version of this article is solely governed by the terms of such publishing agreement and applicable law.

© The Author(s), under exclusive licence to Springer Nature Limited 2025

Methods

Mice

All mice were purchased from The Jackson Laboratory. Six-to-eight-week-old wild-type C57BL6/J male or female mice (000664, The Jackson Laboratory) were group housed 3–5 in a cage with unlimited access to food and water, unless mice were water-restricted for the behavioural assays, in which mice were given a total of 1 ml of water per day. Mice were housed at 72 °F (22.2 °C) and 30–70% humidity in a 12-h light–dark cycle. For CRISPR experiments, 6–8-week-old male or female *Rosa26-LSL-Cas9* knock-in mice (024857, Jackson Laboratories) were housed under the same conditions. All procedures were done in accordance with guidelines approved by the Institutional Animal Care and Use Committees (protocol no. 22087H) at The Rockefeller University. The number of mice per experiment was determined on the basis of expected variance and effect size from previous studies, and no statistical method was used to predetermine sample size. For behavioural experiments, mice were counterbalanced by sex and scored with automated MATLAB scripts, but experimenters were not blinded to group identity.

Surgeries

All surgical procedures and viral injections were carried out under protocols approved by The Rockefeller University Institutional Animal Care and Use Committee. Mice were anaesthetized with 1–2% isofluorane for the entire duration of the procedure and positioned on a Kopf stereotactic apparatus with a heating pad. Puralube Vet Ointment was applied to the eyes to prevent drying, and 0.2 mg kg^{-1} meloxicam was administered intraperitoneally using a 1-ml syringe and 23-G needle. Hair from the scalp was trimmed, and the area was sterilized with povidone–iodine and ethanol. A midline incision was made with a sterile scalpel and holes for injection sites were made using a sterile 0.5-mm micro drill burr (Fine Science Tools) through the skull. All viral injections were performed using a 24-G beveled needle (World Precision Instruments) in a 10-µl NanoFil Sub-Microliter Injection syringe (World Precision Instruments) controlled by an injection pump (Harvard Apparatus) at a rate of 100 nl min^{-1}. Following viral injection, the needle was raised to 0.1 mm above the injection site for 3 min (to prevent backflow) before being slowly raised out of the skull. We used 4-0 vicryl and Vetbond (3 M) to close the incision. For mice used for head-fixed behaviour, a custom titanium headplate was adhered to the skull with Metabond. For mice that required cannulas, the cannulas were implanted immediately following viral injection. Animals were allowed to recover on a heating pad for 1 h and given meloxicam tablets. Following viral injections, mice were kept for 3 weeks to allow adequate expression of the viral construct before behavioural testing or histology.

Viral injections

The following coordinates were used: −1.5 mm anteroposterior (AP), ±1.5 mm mediolateral (ML) and −1.5 mm dorsoventral (DV) for the CA1 region; +1.0 mm AP, ±0.35 mm ML and −1.4 mm DV for the ACC; −0.85 mm AP, ±0.6 mm ML and −3.55 mm DV for the ANT; −4 mm AP, ±3.75 mm ML and −4.2 mm DV for the entorhinal cortex (EC); −2 mm AP, ±0.4 mm ML and −0.5/−0.8 mm DV for the retrosplenial cortex (RSC); and −1.3 mm AP, ±3 mm ML and −4.5 mm DV for the basolateral amygdala (BLA).

In the stGtACR2 inhibition experiments, 900 nl of rgAAV-hSyn-Cre (105553, Addgene; 1.3×10^{13} vg ml^{-1}) was injected bilaterally in the ACC and 900 nl of AAV1-hSyn1-SIO-stGtACR2 (105677, Addgene) was injected bilaterally in the ANT, EC, BLA and RSC. pAAV1-CKIIa-stGtACR2-FusionRed (105669, Addgene) was injected bilaterally in the ACC or CA1 region of the HPC.

In the stabilized step-function opsin experiments, 900 nl rgAAV-hSyn-Cre (1.3×10^{13} vg ml^{-1}) was injected bilaterally in the ACC and 600 nl AAV-Ef1a-DIOhChR2(C128S/D156A)-eYFP (Vector BioLabs; 1.0×10^{13} vg ml^{-1}) was injected bilaterally in the ANT.

In the CRISPR–Cas9 knockout experiments, 600 nl of AAV9:ITR-U6-sgRNA-hSyn-Cre-2A-eGFP (60231, Addgene; 1.0×10^{12} vg ml^{-1}) was injected bilaterally in the ANT or 900 nl was injected bilaterally in the ACC. For experimental controls, 600 nl of AAV9-Cre (1.0×10^{11} vg ml^{-1}) was injected bilaterally in the ANT or ACC.

In the photometry experiments, *Rosa26-LSL-Cas9* control mice were injected with 800 nl AAV9-CAMKIIa-jGCaMP8m (176751-AAV9, Addgene; 5×10^{12} vg ml^{-1}) contralaterally in the ANT and ACC. *Rosa26-LSL-Cas9* mice for knockout testing were additionally injected with 500 nl AAV9:ITR-U6-sgRNA-hSyn-Cre-2A-eGFP (60231, Addgene; 1.0×10^{12} vg ml^{-1}) bilaterally in the ANT.

Cannula implants

For optogenetics, surgeries were carried out as previously described. Immediately after viral injection, animals were implanted with fibre optic cannulas (Doric Lenses). Mice were implanted bilaterally with 200-µm diameter cannulas (0.22 NA; Doric Lenses). Cannula implants were slowly lowered using a stereotaxic cannula holder (Doric) at a rate of 0.001 mm s^{-1} reaching 0.2 mm dorsal to the injection site. Throughout the implantation procedure, the injection area was continually flushed with 0.9% saline and suctioned. Optic glue (Edmund Optics) was then used to secure the cannula to the skull surface, and a custom titanium headplate was affixed as previously described.

For photometry, mice were contralaterally implanted with 1.25-mm ferrule-coupled optical fibres (0.48 NA, 400 µm diameter; Doric Lenses) cut to the desired length so that the implantation site was approximately 0.2 mm dorsal to the injection site in the ANT and ACC.

Optogenetic manipulations

Optogenetic inhibition. For projection-specific expression of stGtACR2, mice were injected with rgAAV-hSyn-Cre (105553, Addgene) bilaterally in the ACC and AAV1-hSyn1-SIO-stGtACR2 (105677, Addgene) bilaterally in the ANT, BLA, EC or RSC. For local inhibition, AAV9-CKIIa-stGtACR2-FusionRed (105669, Addgene) was injected bilaterally in the ACC or HPC. Control cohorts were injected with rgAAV-hSyn-Cre (172221, Addgene) in the ACC and AAV9-hSyn-mCherry (114472, Addgene). Volumes and titres were previously described. A blue 470-nm light was delivered during the cue zones of training sessions (at a power of 15 mW measured at the fibre tip). No inhibition was carried out during retrieval sessions.

Optogenetic activation. For activation of ANT–ACC projections, mice were injected with rgAAV-hSyn-Cre bilaterally in the ACC and pAAV-Ef1a-DIOhChR2(C128S/D156A)-eYFP bilaterally in the ANT. Dual fibre optic cannulas were implanted in the ANT. At the beginning of each training session, a blue 470-nm light was on for 5 s (at a power of 15 mW measured at the fibre tip), and at the end of each session, a secondary pulse of yellow light at 589 nm was administered to deactivate the stabilized step-function opsin and return the membrane potential of transfected neurons to resting values.

Histology

Mice were transcardially perfused with 20 ml cold PBS and 20 ml cold 4% paraformaldehyde (in PBS). Brains were submerged in 4% paraformaldehyde at 4 °C overnight. The next day, brains were submerged in a 30% sucrose (dissolved in PBS) for 24 h at 4 °C. For histology, brains were sliced into 60-µm coronal sections using a freezing microtome (SM2010R, Leica) and stored in 1× PBS. For immunostaining, fixed brain sections were blocked in solution of 3% normal donkey serum, 5% BSA and 0.2% Triton X-100 in 1× PBS for approximately 3 h and incubated with primary antibody overnight at 4 °C. Sections were washed three times in PBS-T (PBS with 0.1% Tween-20) and incubated in the appropriate secondary antibody for approximately 2.5 h at room temperature.

Following 3 × 5 min washes in PBS-T, free-floating sections were stained with DAPI (1:1,000 in PBS-T) and mounted on slides with ProLong Diamond Antifade Mountant (Invitrogen). Images were acquired at ×10 and ×20 magnification with a Nikon inverted microscope (Nikon Eclipse Ti). Primary antibodies included Cre recombinase (D7L7L) XP rabbit monoclonal antibody (15036, Cell Signaling Technology; 1:100 dilution), CREB (48H2) rabbit monoclonal antibody (9197, Cell Signaling Technology; 1:50 dilution) and anti-CAMTA1 rabbit polyclonal antibody (SAB4301068, Millipore Sigma; 1:100 dilution). Secondary antibodies included Alexa Fluor 647-conjugated AffiniPure donkey anti-rabbit IgG (711-605-152, Jackson ImmunoResearch; 1:250 dilution) and AlexaFluor 647-conjugated AffiniPure donkey anti-mouse (715-606-151, Jackson ImmunoResearch).

Behaviour

Virtual reality system. For the behavioural experiments, we used a custom-built virtual reality environment by adapting a previously reported task[26]. In brief, a 200-mm-diameter styrofoam ball was axially fixed with a 6-mm-diameter assembly rod (Thorlabs) passing through the centre of the ball and resting on 90° post-holders (Thorlabs) at each end, allowing free forwards and backwards rotation of the ball. Mice were head fixed in place above the centre of the ball using a head-plate mount (Thorlabs). Virtual environments were designed in the virtual reality MATLAB engine ViRMEn. The virtual environment was back projected (Kodak Ultra Mini Portable Projector) onto white fabric stretched over a clear acrylic hemisphere with a 14-inch diameter placed approximately 20 cm in front of the centre of the mouse, encompassing 220° of the field of view of the mouse. The rotation of the styrofoam ball was recorded by an optical computer mouse (Logitech) that interfaced with ViRMEn to transport the mouse through the virtual reality environment. A National Instruments Data Acquisition (NIDAQ) device was used to record lick events (as capacitance changes on the lick port) and to trigger the various Arduinos controlling tones, odours and air puff, as well as optogenetic stimuli.

Behavioural shaping. Mice were put on a restricted water schedule, receiving 1 ml of water per mouse on a given day. Body weight was monitored daily to ensure it was maintained above 80% of the pre-restriction measurement. After 3 days of water deprivation, mice were habituated to the Styrofoam ball for 5 days by receiving their 1 ml of water per day while head fixed. During the habituation protocol, mice proceeded on a linear track through a start zone, then a cue zone, where an auditory cue was delivered (Hz), after which they entered an outcome zone to receive 5 s of water delivery. If a mouse did not drink 1 ml of water, it was supplemented with water that day to a total of 1 ml. By the end of the shaping protocol, all mice learned to lick to retrieve water in the outcome zone. After 5 days of the shaping protocol, training began.

Behavioural training. The trial structure consisted of three zones on a linear track: (1) start, (2) cue, and (3) outcome zone. Each trial was initiated in a neutral start zone (linear track). Next, mice were transported to a cue zone where they learned to use contextual cues to predict the paired reward (water) or punishment (air puff to the snout) in the outcome zone. The contextual cues consisted of visual cues (colours and shapes on the walls of the track), auditory cues outputted by a thin plastic speaker (Adafruit), and olfactory cues (released from a custom-built olfactometer). The visual cues were generated within the ViRMEn GUI, and both auditory and olfactory cues were outputted by Arduino code under the control of ViRMEn code. The contexts used were: (1) reward-HR (yellow rectangles for visual, isoamyl acetate for odour, 5 kHz tone for auditory), (2) reward-LR (pink hexagons, benzaldehyde, 7 kHz tone), and (3) aversive (blue triangles, octanal, 9.2 kHz). All three contexts were interleaved and randomized on training days. The HR context appeared with approximately 50% frequency, the LR context appeared with approximately 22% frequency, and the aversive context appeared with approximately 28% frequency.

After the cue zone, mice were transported to an outcome zone. On reward trials, they received water if they made contact with the lick port. After the aversive cues, two air puffs (35 psi) were released by a solenoid (Precigenome, isolation valve, 20NC, 0.032″ (0.8 mm) orifice, diaphragm, 2-way) controlling airflow into a pipette tip placed 1 cm away from the snout. Although mice could self-initiate movement on the ball, which would generate visual movement down the VR track, they were transported through the rooms on a timed schedule, regardless of the distance they ran on the ball. For a single trial, mice were transported through a neutral start track (8 s), cue zone (5 s) and outcome zone (5 s) in training, resulting in 40–50 trials per session. In retrieval, durations were slightly shorter in the neutral start zone (5 s), cue zone (5 s) and outcome zone (3 s), resulting in 20–30 trials per session.

Performance on the task was assessed by average anticipatory lick rate measured from the last 2 s of the cue zone immediately preceding the outcome zone. Mice were trained for 7–9 days, depending on when they met learning criteria (discrimination index ≥ 0.3). During training, reinforcement (air puff or water) was always paired to the outcome zone. By contrast, during retrieval, mice were not presented with any reinforcement in the outcome zone. Thus, during retrieval, both anticipatory licking and licking during the outcome zone were measured. For some longitudinal experiments requiring testing over multiple retrieval days, mice had to be retrained on the task to avoid memory extinction and loss of engagement in the task in future time points. Immediately following testing on the same day, these mice received 10 min of a 'retraining' session where reinforcement (water or puff) was re-introduced.

The overall time course of the behaviour consisted of the following phases: habituation (5 days), training (T1–T7 or up to T9) and retrieval (R1–R30). During the habituation phase, each mouse was habituated for 15 min. During the training phase, each mouse was trained for 15–17 min per session. During the retrieval phase, mice were tested for 5–6 min. Recent retrieval was defined by retrieval days R1–R7 following the final day of training. Mid-retrieval was defined by retrieval days R8–R14 and remote retrieval was defined by retrieval days R15–R30 following the final day of training. We refer to R20 ACC single-cell RNA sequencing (scRNA-seq) samples as 'late remote' to differentiate from R15 samples.

Behavioural analysis. In all behavioural experiments, we assessed learning and memory recall by calculating the average lick rate difference, which we refer to as the discrimination index (DI). The discrimination index was calculated as follows:

$$\mathrm{DI} = \frac{\text{mean lick rate in reward context} - \text{mean lick rate in aversive context}}{\text{mean lick rate in reward context} + \text{mean lick rate in aversive context}}$$

A discrimination index (DI) of +1 therefore indicates perfect discrimination (licking only in reward and no licking in aversive cue zones), whereas a discrimination index of 0 indicates chance performance (equal licking in reward and aversive cue zones). DI was calculated as either HR over aversive or LR over aversive. For training sessions, the lick rate was calculated only in the window of 2 s preceding entry into the outcome zone where reinforcement (water or air puff) was delivered (termed anticipatory licking). On retrieval sessions, we included lick rates 1 s before the outcome and during the entire 3 s of outcome zone, as no reinforcement (water or air puff) was provided in the outcome zone. For behavioural experiments in which mice recalled a single reward context during retrieval (either HR or LR), a DI could not be calculated. Therefore, we used the area under the lick rate curve, calculated over a window 2 s preceding the start of the outcome

zone and over the entire outcome zone of 3 s, to assess performance. The area under the curve was calculated as follows:

$$\int \text{average lick ratecurve}$$

Cell culture. The mouse neuroblastoma Neuro2a cell line was obtained directly from the American Type Culture Collection (CCL-131), and no additional cell line authentication was performed. The cell cultures were maintained at 37 °C in a 5% CO_2 atmosphere. For guide RNA testing, cells were plated at 60% confluency in tissue culture-treated 24-well plates (3524, Corning) and transfected using Lipofectamine 3000 Transfection Reagent (Thermo Fisher Scientific) following the manufacturer's protocol. Neuro2a cells were cultured in DMEM medium (high glucose with L-glutamine and sodium pyruvate) containing 10% FBS (Gibco) and 1% antibiotic–antimycotic (Gibco). All cell cultures were tested regularly for mycoplasma contamination with a mycoplasma PCR detection kit (ThermoFisher).

CRISPR–Cas9

sgRNA design and validation. To design sgRNAs for CRISPR–Cas9 knockout with minimal off-target effects and targeting early exons, 3–8 sgRNAs targeting the protein-coding sequences of selected genes were selected from either CHOPCHOP (http://chopchop.cbu.uib.no) or CRISPick (https://portals.broadinstitute.org/gppx/crispick/public). To select the most efficient sgRNAs per gene, in vitro knockout efficiency was assessed by transfecting Neuro2a neuroblastoma cells with pSpCas9(sgRNA)-2A-GFP (172221, Addgene; 1,000 ng) using Lipofectamine 3000 Transfection reagent. Neuro2a cells were seeded at 60% confluency in a six-well plate format and transfected over 48 h, before sorting for $eGFP^+$ cells. DNA was isolated from sorted cells (T3010, New England Biolabs) and loci-specific primers were used to PCR amplify around the edited region with Q5 High-Fidelity 2X Master Mix (M0492, New England Biolabs). The DNA band of expected size was agarose gel purified (T1120, New England Biolabs) and cleaned up samples were submitted for Sanger sequencing with forward primer (Supplementary Table 6), followed by Synthego ICE Analysis (https://ice.synthego.com/#/) to assess cutting efficiency. DNA amplicons were sequenced using EZ amplicon sequencing (Genewiz) and the percentage of indels calculated. The most efficient guides per gene tested in vitro were selected for cloning into AAV:ITR-U6-sgRNA(backbone)-hSyn-Cre-2A-eGFP-KASH-WPRE-shortPA-ITR (pAAV60231; 60231, Addgene). Plasmids to be used in vivo were serotyped with AAV9 coat proteins and packaged by the University of Arizona Viral Core (at 10×10^{13} GC ml^{-1} viral titres).

sgRNA cloning. For in vivo sgRNA design, the sgRNAs were synthesized individually (Integrated DNA Technologies) and cloned into the sgRNA-expressing AAV vector (AAV:ITR-U6-sgRNA(backbone)-hSyn-eGFP-KASH-WPRE-shortPA-ITR; #60231, Addgene). In brief, oligonucleotides (Supp) for each sgRNA were phosphorylated and annealed by T4 polynucleotide kinase (New England Biolabs). The sgRNA backbone was digested with SapI (New England Biolabs), and annealed sgRNA inserts were cloned into the backbone by Golden Gate assembly. Then, assembly reactions were transformed into stable-competent *Escherichia coli* (C3040H, New England Biolabs). To verify the sgRNA insert sequences, the sgRNA were Sanger sequenced from the U6 promoter using the U6-fwd primer (Supplementary Table 6). For in vitro validation and selection of guides, the same steps were carried out, except the oligos were designed with BbsI overhangs and cloned into the sgRNA backbone, pSpCas9(BB)-2A-GFP Px458 (Addgene plasmid 48138) with BbsI-HF digestion before Golden Gate assembly (New England Biolabs).

In vivo sgRNA validation. To confirm sgRNA targeting in vivo, *Rosa26-LSL-Cas9* mice were injected with pAAV60231-sgRNA (#60231, Addgene) were housed for 3 weeks after injection to allow for adequate expression. Then, tissue from the ANT or ACC was collected by removing the brain and slicing into 500-µm sections. The brain regions were collected using fluorescence-aided dissection. Tissue sections were either flash frozen in liquid nitrogen or processed immediately. Nuclear isolation proceeded as follows: dissected sections were collected into 500 µl of 54% Percoll buffer. The tissue was homogenized by pipetting with a P1000, followed by a 23-G syringe and a 27-G syringe. Five microlitres of 10% NP-40 and 5 µl of 10% Tween-20 (11332465001, Millipore Sigma) were added to the sample and mixed by pipetting. Samples were placed on ice for 15 min, after which 500 µl of 1× buffer, cOmplete EDTA-free protease inhibitor cocktail (11836170001, Fisher Scientific), was added to the tissue. We added 200 µl of 31% Percoll buffer followed by 100 µl of 35% Percoll buffer to the bottom of the tube, creating a buffer gradient. The samples were centrifuged using a swing rotor at 20,000 *g* and 4 °C for 10 min. The bottom 100 µl was collected from the bottom layer and blocked by adding 50 µl of 5% BSA–PBS for 5 min on ice. Then, the sample was incubated with primary antibody anti-GFP (BioLegend) at a concentration of 1:2,000 for 15 min on ice. The sample was then washed with 1,000 µl of 1× PBS and centrifuged at 500*g* for 5 min and the supernatant was removed, followed by resuspension in FACS buffer (1× PBS, 1% FBS, 0.05% sodium azide). Cells were sorted for GFP^+ and DNA from nuclei was isolated (New England Biolabs, see Supplementary Fig. 2d for gating strategy). To detect the percentage indel frequency near the targeted site, primers flanking the deleted region (Supplementary Table 6) were used to amplify the intervening region by PCR from genomic DNA, and the product was Sanger sequenced. Primers were designed to flank a region between 300 bp and 500 bp encompassing the sgRNA sequence. Samples were also set for whole-amplicon sequencing (next-generation sequencing) for more detailed mutational characterization.

qPCR

To validate the behavioural results of the scRNA pseudotime, an independent behavioural cohort was prepared and qPCR was performed on tissue dissected from animals for early (R2–R8) or late (R20) time points, exposed to either HR or LR contexts during retrieval ($n = 3$ or $n = 6$ mice per condition). Animals were euthanized within 60 min of the end of behavioral testing and samples were snap frozen on liquid N_2. To validate targets of transcriptional regulators, an entirely separate cohort was prepared, where tissue was dissected from control (*Cre*) or knockout animals (*Ash1l* in the ACC, and *Tcf4* and *Camta1* in the ANT). Animals were tested on retrieval on R8 (for *Camta1* and controls) or R20 (*for Tcf4*, *Ash1l* and controls).

Total RNA was extracted from dissected brain tissue using the Total RNA Purification Kit (Norgen Biotek), following the manufacturer's protocol, with column-based genomic DNA removal to eliminate genomic DNA contamination. RNA concentration and integrity were assessed using an Agilent Bioanalyzer and NanoDrop spectrophotometer. Complementary DNA (cDNA) was synthesized from 500 ng to 1,000 ng of RNA using the iScript cDNA Synthesis Kit (Bio-Rad) in a 20 µl reaction volume. Primer pairs were designed using NCBI Primer-BLAST to amplify target regions of 80–150 bp, with melting temperatures optimized to 60 ± 1 °C and GC content between 40% and 60% (Supplementary Table 6). The specificity of the primers was confirmed by melt curve analysis conducted over a temperature range of 65–95 °C with 0.5 °C increments. Primer efficiency was validated using a standard curve generated from tenfold serial dilutions of pooled cDNA, ensuring efficiencies between 90% and 110% and an $R^2 > 0.98$.

qPCRs were performed in technical triplicates using a QuantStudio 3 Real-Time PCR System, following a 96-well plate format. A master mix was prepared from 2X SYBR Green qPCR Master Mix (Thermo Fisher), nuclease-free H_2O, and forward and reverse primers, following the manufacturer's protocol (Supplementary Table 6). Each final reaction consisted of 17 µl total volume, composed of 15 µl of the master

mix and 2 µl of cDNA template. The cycling conditions included an initial denaturation step at 95 °C for 3 min, followed by 45 cycles of denaturation at 95 °C for 10 s and annealing/extension at 60 °C for 30 s. Melt curve analysis was performed immediately after amplification to confirm primer specificity. Relative quantification of gene expression was calculated using the comparative ΔΔCt method, with normalization to *Map2* as the housekeeping gene, and HR samples normalized to the average of LR samples as a baseline of 1. Genes for which Ct > 35 were not used. Statistical analyses were performed using GraphPad Prism v9 software. Differences between experimental groups were assessed by a one-tailed, parametric, unpaired Student's *t*-test, with significance defined as $P < 0.05$. Data are presented as mean ± s.e.m. from 3 to 6 independent biological replicates.

Western blot

To validate CRISPR knockdown from dissected brain tissue, animals were euthanized 3 weeks post-surgery, and the injected region was carefully dissected with fluorescence-guided microdissection. Brain tissue was lysed using a lysis buffer consisting of 7 ml of RIPA buffer, 70 µl of 100 mM PMSF and Halt protease inhibitor (Thermo Fisher). Tissue samples were placed in a 1.5-ml Eppendorf tube containing 228 µl of lysis buffer and finely minced into small pieces using spring scissors. The minced tissue was homogenized by passing it through a 23-G insulin syringe ten times to ensure uniform suspension. An additional 228 µl of lysis buffer and 45 µl of 10% SDS were added to achieve a final SDS concentration of 1%. The mixture was passed through the syringe an additional five times. The homogenized sample was heated at 95 °C for 5 min to denature proteins, then cooled on ice for 15 min. Samples were rotated end-over-end at room temperature for 40 min. Following lysis, samples were centrifuged at 20,000*g* for 20 min at 4 °C to pellet debris. The supernatant was carefully collected and protein concentration was measured with the Pierce BCA Protein Assay kit and quantified by Nanodrop.

Western blotting was performed using the Odyssey XF Imaging System (LI-COR Biosciences). Cells were lysed in a cold RIPA supplemented with Halt protease inhibitor cocktail (Thermo Fisher), and protein concentrations were determined using a Pierce BCA Protein Assay kit and quantified by Nanodrop. Protein samples (20 µg) were denatured by heating at 95 °C for 5 min in 4X SDS sample buffer with 100 mM dithiothreitol and resolved by SDS–PAGE. Proteins were then transferred onto PVDF membranes using a wet transfer system at 70 V for 2 h. Membranes were blocked in Odyssey Blocking Buffer (PBS based) for 1 h at room temperature. Following blocking, membranes were incubated overnight at 4 °C with primary antibodies specific to *Tcf4* (PA5-88125, Thermo Fisher) diluted 1:1,000 and α-tubulin (2144, Cell Signaling Tech) in Odyssey blocking buffer containing 0.1% Tween-20. After three washes with PBS-T, membranes were incubated with IRDye 800CW goat anti-rabbit IgG or IRDye 680RD goat anti-mouse IgG, diluted 1:15,000 in Odyssey blocking buffer + 0.1% Tween-20 for 1 h at room temperature in the dark. Membranes were washed three additional times with PBST and imaged while wet on the Odyssey XF Imaging System. Protein bands were visualized in the 700-nm and 800-nm channels.

Nuclear extraction for ATAC-seq

Mice were euthanized within 40–60 min from the end of behavioural testing. The ANT and ACC of C57BL6/J mice were dissected, and nuclei were extracted using the Percoll gradient method. The dissected tissue was homogenized with 54% Percoll (Cytiva) in 1× buffer (50 mM Tris-HCl pH 7.4, 25 mM KCl, 5 mM $MgCl_2$ and 250 mM sucrose) on ice, using a 23-G syringe and a 27-G syringe, 10 strokes each. After homogenization, 10% NP-40 substitute (11332473001, Roche) and 10% Tween-20 were added and incubated for 15 min on ice (0.1% final concentration for both NP-40 and Tween-20). Following the incubation, an equal volume of 1× buffer was added and mixed by pipetting. A Percoll gradient was prepared by layering 31% and 35% Percoll at the bottom of the tube. Nuclei were pelleted in the bottom layer by centrifugation in a swinging bucket (14,000*g* for 10 min at 4 °C). The nuclear pellet was carefully resuspended in blocking buffer (5% BSA–PBS) and incubated for 10 min on ice. After blocking, nuclei were labelled by incubation with Alexa Fluor 488-conjugated anti-NeuN antibody (1:2,000) for 20 min on ice. Nuclei were then washed once in PBS and labelled with 7-AAD (SML1633, Sigma). The 7-AAD singlet and NeuN-positive population was sorted by FACS, and the sorted nuclei were used for ATAC-seq (for FACS gating strategy, see Supplementary Fig. 2b).

ATAC-seq

Mice were euthanized within 40–60 min from behavioural testing. ATAC-seq preparation was performed as previously described[50]. NeuN-positive nuclei ($2–5 \times 10^4$) were isolated by FACS and treated with Tn5 transposition mix (Illumina) at 37 °C for 30 min in a thermomixer (Eppendorf) at 1,000 rpm mixing. After the Tn5 reaction, DNA was extracted with DNA Clean and Concentrator-5 Kit (D4013, Zymo Research) and amplified with NEBNext Ultra II Q5 2× Master Mix (M0544L, New England BioLabs). Amplified DNA was extracted using a DNA Clean and Concentrator-5 Kit (D4013, Zymo Research) and DNA concentration was quantified by NEBNext Library Quant Master (E7630S, New England BioLabs). The quality of the purified DNA was checked with a BioAnalyzer (Agilent), and the DNA was sequenced with an Illumina NovaSeq S2 system (50 bp, paired end).

Pre-processing. Paired sequencing reads were 3′ trimmed and filtered for quality ($Q \geq 15$) and adapter content using v0.4.5 of TrimGalore, v1.15 of cutadapt and v0.11.5 of FastQC. Bowtie2 v2.3.4.1 was used to align reads to mouse assembly mm10 with and duplicates were collapsed to one read using MarkDuplicates in v2.16.0 of Picard Tools. Enriched regions were discovered using MACS2 with a *P* value setting of 0.001, filtered for blacklisted regions (http://mitra.stanford.edu/kundaje/akundaje/release/blacklists/mm10mouse/mm10.blacklist.bed.gz), and a peak atlas was created using ±250 bp around peak summits.

ATAC-seq analysis. featureCounts v1.6.1 was used to build a raw counts matrix and DESeq2 was used to calculate differential enrichment (fold change ≥ 2 and false discovery rate (FDR)-adjusted $P \leq 0.05$) for all pairwise contrasts. The BEDTools suite was used to create bigwig files normalized using the DESeq2 sizeFactors, which were also used to normalize the raw counts matrix. Peak–gene associations were created by assigning all intragenic peaks to that gene, whereas intergenic peaks were assigned using linear genomic distance to transcription start site. Volcano plots were generated using the EnhancedVolcano() package in R with pCutoff = 0.002 and FCcutoff = 1. Network analysis was performed using the assigned genes to differential peaks by running enrichplot::cnetplot in R with default parameters. Motif signatures were obtained using Homer v4.5 on differentially enriched peaks. Heatmaps of ATAC peaks for the transcriptional regulators and their modules were generated using normalized counts filtered by log fold change > 0 from the between R8 versus homecage pairwise comparison.

scRNA-seq

Single-cell dissociation and scRNA-seq. Single-cell suspensions of ACC and ANT were prepared as previously described[51]. In brief, mice were euthanized within 40–60 min from behavioural testing with an overdose of isoflurane followed by transcardial perfusion with carbonated (95% O_2 and 5% CO_2) Hanks' balanced salt solution containing a small-molecule cocktail consisting of 1 µM tetrodotoxin (Sigma), 100 µM AP-V (Thermo Fisher Scientific) and 5 µg actinomycin D (Sigma) per millilitre and 10 µM triptolide (Sigma) to optimize for preserving transcriptional states. Brains were removed, 500-µm sections were collected and the region of interest was dissected. The tissue was dissociated using papain (LS003124, Worthington) dissolved in Hibernate A buffer (NC1787837, Fisher Scientific) containing 1 µM tetrodotoxin,

100 µM AP-V (Thermo Fisher Scientific), 5 µg actinomycin D (Sigma) per millilitre, 10 µM triptolide (Sigma) and 10 µg anisomycin (Sigma) per millilitre, and incubated for 25–30 min at 37 °C, followed by manual trituration using fire-polished Pasteur pipettes and filtering through a 40-µm cell strainer (BAH136800040, Millipore Sigma). Cells were washed with a wash buffer (PBS + 1% BSA) and centrifuged at 500*g* for 5 min, the supernatant was carefully removed, and cells were resuspended in approximately 500 µl wash buffer and 10% DAPI. Flow cytometry was performed using a BD FACS Aria III Cell Sorter (BD FACSDiva Software v8.0.1) with a 100-µm nozzle. The cell suspensions were first gated on forward scatter, then within this population based on DAPI-negative cells. Cells were collected in wash buffer, manually counted using a Burker chamber, and suspension volumes were adjusted to a target concentration of 700–1,000 cells per microlitre. scRNA-seq was carried out with the Chromium Next GEM Single Cell 3′ Kit v3.1 (1000268, 10X Genomics). Manufacturer's instructions were followed for downstream cDNA synthesis (12–14 PCR cycles) and library preparation. Final libraries were sequenced on the Illumina NovaSeq S4 platform (R1 for 28 cycles, i7 for 8 cycles and R2 for 90 cycles).

ChIP–seq

In vitro ChIP antibody validation. Wild-type and knockout Neuro2A cell lines were generated and used to choose the most optimal antibody for ChIP–seq. In brief, 1×10^7 Neuro2A cells were transfected with Px458-*Tcf4*-sgRNA (#48138, Addgene) or Px458-*Camta1*-sgRNA (#48138, Addgene) for 72 h and harvested. Freshly harvested cells were fixed with 1% formaldehyde for 10 min, after which the reaction was quenched by the addition of glycine to the final concentration of 0.125 M. Fixed cells were washed twice with PBS, snap frozen and stored at −80 °C.

Behaviour for ChIP–seq experiment. For in vivo ChIP experiments, an independent behavioural cohort was run according to the behavioural task above. Cohorts of *Rosa26-LSL-Cas9* animals were injected with either *Ash1l*-targeting sgRNA, *Tcf4*-targeting sgRNA or *Camta1*-targeting sgRNA. For assessing the histone methylation landscape over time, both control animals and *Ash1l*-knockout animals were tested on R2, R8 and R20. For *Camta1* knockout and *Tcf4* knockout, animals were tested and euthanized on R8. For *Ash1l* knockout and controls used for H3K4me3 ChIP, two independent biological replicates were included, each pooled from tissue dissected from three to four animals. For *Camta1* knockout and *Tcf4* knockout (and corresponding R8 controls), one biological replicate was included, each pooled from nine mice to obtain enough cells for downstream ChIP–seq for those specific antibodies, as determined by the in vitro ChIP input (Supplementary Table 5).

Nuclei isolation of neurons for ChIP–seq. Animals were anaesthetized with isoflurane within 40–60 min of performing the task retrieval and perfused with PBS. ANT or ACC tissue was microdissected under a microscope and snap frozen on liquid nitrogen for later processing. Nuclei were isolated from mouse brain tissue based on a previously described method[52] with slight modifications. Tissue from $n = 8–9$ mice was pooled for *Camta1* knockout and *Tcf4* knockout and their respective controls, and tissue from $n = 2–3$ mice was pooled for each biological replicate for *Ash1l*-knockout. In brief, 0.3 ml fixative solution (1% (wt/vol) formaldehyde in DPBS) was added to the pooled sample (approximately 60–80 mg tissue) in a 1.5-ml tube. Tissue was gently homogenized in the fixative by gently breaking up with a P1000 pipette tip until no large visible pieces remained. For *Ash1l* samples, the 0.3 ml homogenate was added to a 4.7 ml fixative solution in a 15-ml tube using a P1000 tip, washing out the 1.5-ml tube to maximize homogenate transfer. Homogenate was rocked at 30 cycles per minute at room temperature for 10 min. To quench the formaldehyde and prevent overfixation of the sample, 0.5 ml 2.5 M glycine (final) = 0.125 M was added to the homogenate and rocked at 30 cycles per minute at room temperature for 5 min. For *Tcf4*-knockout and *Camta1*-knockout samples, a double fixation protocol was used: homogenization of sample in 0.3 ml 2 mM DSG solution, followed by transfer to 4.7 ml 2 mM DSG, rocked at 30 cycles per minute at room temperature for 30 min. Formaldehyde (37% wt/vol) was added to the homogenate to create a 1% (wt/vol) formaldehyde solution, rocked for 10 min at room temperature. The sample was quenched with 0.125 M glycine. After fixation and quenching, the rest of the steps were the same. The homogenate was spun at 1,100*g* for 5 min at 4 °C in a swing rotor bucket centrifuge with 15-ml adaptors. Supernatant was removed and pellet was suspended with 10 ml ice-cold NF1 buffer (10 mM Tris-HCl pH 8.0, 1 mM EDTA, 5 mM $MgCl_2$, 0.1 M sucrose and 0.5% (vol/vol) Triton X-100) for a first wash. This was repeated for a second wash, and on the third (final), the sample was resuspended in 5 ml ice-cold NF1 buffer. Homogenate was incubated on ice for 30 min, then transferred to a 7-ml glass dounce. A loose pestle was passed through the homogenate 20×, and then a tight pestle passed through 5×. The homogenate was passed through a 70-µm strainer and collected into a 50-ml tube. An additional 15 ml NF1 buffer was passed through the strainer to collect a total volume of 20 ml. A 5 ml sucrose cushion (1.0 M sucrose cushion with 1.2 M sucrose solution with 10 mM Tris-HCl pH 8.0, 3 mM $MgCl_2$ and 1 mM dithiothreitol) was laid underneath the homogenate by slowly pipetting to the bottom of the tube with a P1000, with care to maintain an interphase. The sucrose gradient was spun at 3,900*g* for 30 min at 4 °C. After spinning, a white nuclei pellet was visible at the bottom, below the sucrose cushion. The upper, aqueous phase, interphase and sucrose cushion were gently removed. The nuclei pellet was resuspended in 1 ml NF1 buffer and transferred to a 15-ml tube. NF1 buffer (9 ml) was added to wash the nuclei pellet, followed by spinning at 1,600*g* for 5 min at 4 °C to pellet the nuclei. For antibody staining for nuclei sorting, the nuclei pellet was resuspended in 5 ml FANS buffer, spun at 1,600*g* for 5 min at 4 °C, and resuspended in 0.3 ml FANS buffer. Three microlitres was taken for an unstained control, and the remaining nuclei were transferred to a FACS tube for staining overnight 4 °C with NeuN-Ax488 antibody (#MAB377X, Millipore) at 1:2,500 dilution with gentle rocking. The next day, 4 ml FANS buffer was added to the nuclei, then spun at 1,600*g* for 5 min at 4 °C. The remaining 0.3 ml nuclei were passed through a 35-µm cap into a new tube for FACS and counterstained with 0.5 µg ml^{-1} DAPI. Nuclei were sorted using a 100-µm nozzle. Nuclei were gated based on $DAPI^+NeuN^+$ according to the original protocol (for representative FACS gating, see Supplementary Fig. 2e). After sorting, nuclei samples were adjusted to 1% (wt/vol) BSA, then spun at 1,600*g* for 15 min at 4 °C to collect nuclei. FANS buffer was removed, and samples were snap frozen on liquid N_2.

ChIP fixation and sequencing. Frozen pellets of fixed cells (in vitro) or fixed, dissociated nuclei (in vivo behaviour) were resuspended in SDS buffer (100 mM NaCl, 50 mM Tris-HCl pH 8.0, 5 mM EDTA, 0.5% SDS and 1× protease inhibitor cocktail from Roche). The resulting nuclei were spun down, resuspended in the immunoprecipitation buffer at 1 ml per 0.5 million cells (SDS buffer and Triton dilution buffer (100 mM NaCl, 100 mM TrisHCl pH 8.0, 5 mM EDTA and 5% Triton X-100) mixed in 2:1 ratio with the addition of 1× protease inhibitor cocktail (#11836170001, Millipore Sigma) and processed on a Covaris LE220+ focused-ultrasonicator to achieve an average fragment length of 200–300 bp with the following parameters: PIP (peak incident power) = 420, duty factor = 30, cycles per burst = 200 and time = 20 min. Chromatin concentrations were estimated using the Pierce BCA Protein Assay Kit (23227, Thermo Fisher Scientific) according to the manufacturer's instructions. The immunoprecipitation reactions were set up in 500 µl of the immunoprecipitation buffer in Protein LoBind tubes (22431081, Eppendorf) and pre-cleared with 50 µl of protein G Dynabeads (10004D, Thermo Fisher Scientific) for 2 h at 4 °C. After pre-clearing, the samples were transferred into new Protein LoBind tubes and incubated overnight at 4 °C with 5 µg of TCF4 (22337-1-AP,

ProteinTech), CAMTA1 (SAB4301068, Millipore) or H3K4me3 antibody (13-0041 or 13-0060, Epicypher). The next day, 50 µl of BSA-blocked protein G Dynabeads were added to the reactions and incubated for 2 h at 4 °C. The beads were then washed two times with low-salt washing buffer (150 mM NaCl, 1% Triton X-100, 0.1% SDS, 2 mM EDTA and 20 mM TrisHCl pH8.0), two times with high-salt washing buffer (500 mM NaCl, 1% Triton X-100, 0.1% SDS, 2 mM EDTA and 20 mM TrisHCl pH 8.0), two times with LiCL wash buffer (250 mM LiCl, 10 mM TrisHCl pH 8.0, 1 mM EDTA, 1% Na-deoxycholate and 1% IGEPAL CA-630) and one time with TE buffer (10 mM Tris-HCl pH 8.0 and 1 mM EDTA). The samples were then reverse crosslinked overnight in the elution buffer (1% SDS and 0.1 M $NaHCO_3$) and purified using the ChIP DNA Clean & Concentrator kit (D5205, Zymo Research) following the manufacturer's instructions. After quantification of the recovered DNA fragments, libraries were prepared using the ThruPLEX DNA-Seq kit (R400676, Takara) following the manufacturer's instructions, purified with SPRIselect magnetic beads (B23318, Beckman Coulter), and quantified using a Qubit Flex fluorometer (Thermo Fisher Scientific) and profiled with a TapeStation (Agilent). The libraries were sent to MSKCC Integrated Genomics Operation core facility for sequencing on an Illumina NovaSeq 6000 (aiming for 30–40 million 100-bp paired-end reads per library).

ChIP–seq data processing and analysis. Paired sequencing reads were 3′ trimmed and filtered for quality ($Q \geq 15$) and adapter content using v0.4.5 of TrimGalore (https://www.bioinformatics.babraham.ac.uk/projects/trim_galore) and running v1.15 of cutadapt and v0.11.5 of FastQC. Bowtie2 v2.3.4.1 (http://bowtie-bio.sourceforge.net/bowtie2/index.shtml) was used to align reads to mouse assembly mm10 with and duplicates were collapsed to one read using MarkDuplicates in v2.16.0 of Picard Tools. Enriched regions were discovered using MACS2 (https://github.com/taoliu/MACS) with a *P* value setting of 0.001, filtered for blacklisted regions (http://mitra.stanford.edu/kundaje/akundaje/release/blacklists/mm10mouse/mm10.blacklist.bed.gz), and a peak atlas was created using ±250 bp around peak summits for ATAC data and the entire enriched region for ChIP data. featureCounts v1.6.1 (http://subread.sourceforge.net) was used to build a raw counts matrix, and DESeq2 was used to calculate differential enrichment (fold change ≥ 2 and FDR-adjusted $P \leq 0.05$) for all pairwise contrasts. The BEDTools suite (http://bedtools.readthedocs.io) was used to create ATAC bigwig files normalized using the DESeq2 sizeFactors, which were also used to normalize the raw counts matrix. For histone modification data, the ChIP signal was normalized to the sequencing depth for uniquely mapped reads, whereas transcription factor ChIP data were normalized to an external spike in by scaling the data inversely to the number of *Drosophila* H2Av reads. Peak–gene associations were created by assigning all intragenic peaks to that gene, whereas intergenic peaks were assigned using linear genomic distance to the transcription start site. Network analysis was performed using the assigned genes to differential peaks by running enrichplot::cnetplot in R with default parameters. Gene set enrichment analysis (GSEA; http://software.broadinstitute.org/gsea) was performed with the pre-ranked option and default parameters by assigning a gene to the single peak with the largest (in magnitude) $\log_2$ fold change associated with it for each paired contrast. Composite and tornado plots were created using deepTools v3.3.0 by running computeMatrix and plotHeatmap on normalized bigwigs with average signal sampled in 25-bp windows and flanking region defined by the surrounding 2 kb. Motif signatures were obtained using Homer v4.5 (http://homer.ucsd.edu) on differentially enriched peaks.

Photometry

Data acquisition and post-processing. A custom multi-fibre photometry setup, as previously described[28], was used to simultaneously record bulk calcium signals from the ANT and ACC while mice performed the virtual reality-based contextual discrimination task. We recorded at 11 Hz with an excitation wavelength of 470 nm. Before each session, mice were head fixed, and each optical cannula was cleaned with 70% ethanol. For analysis, the images captured were post-processed using custom MATLAB scripts. Regions of interest were manually drawn for each fibre to extract fluorescence values throughout the experiment. Raw signals were high-pass filtered and then *Z*-scored.

Data analysis. All subsequent photometry data analysis was carried out using custom Python scripts. To calculate Pearson correlations between the ANT and ACC, signals from the cue and reinforcement zone were concatenated. To focus on correlations between relevant calcium events rather than noise, only signals above a 0.5 magnitude were used. Pearson correlations were then calculated using the Scipy pearsonr function. To estimate mutual information between the ANT and ACC within each session, the Scikit-learn function mutual_info_regression was used. Finally, to assess the complexity of local ANT and ACC calcium signals across experimental groups, sample entropy was calculated using the AntroPy sample_entropy function with embedding dimension (m) = 2 and tolerance (r) = 0.2.

scRNA-seq data analysis

Quality control and visualization. RAW sequencing reads were aligned to the GRCm38 or mm10 mouse reference genome and all scRNA-seq datasets were initially processed individually using the Sequence Quality Control (SEQC) package[53]. The SEQC pipeline performs cell barcode and unique molecular identifier correction to generate a count matrix (cells × genes); true cells were distinguished from empty droplets based on the cumulative distribution of total molecule counts, and cells with a high fraction of mitochondrial molecules were filtered (more than 20%), as these are probably apoptotic. The Python Scanpy package (v1.9.3) was used to further analyse the data[54]. The presence of doublets was verified again using Scrublet (v0.23)[55] and cell barcodes from Cellplex (1000261, 10X Genomics) were identified for each biological replicate. After this initial preprocessing, samples from all time points were merged (Extended Data Fig. 2d,f). Cells with less than 1,500 unique molecular identifiers per cell and less than 1,000 genes per cell, and genes detected in less than 10 cells were removed. Standard median library size normalization followed by log transformation (pseudo-count = 1) was applied on the data. Ribosomal and mitochondrial genes were removed. Next, highly variable gene (HVG) selection was performed using the scanpy.pp.highly_variable_genes() function in Scanpy with the seurat_v3 method on raw gene expression counts, and principal component analysis was applied to reduce the dimensionality to 30 principal components to obtain 4,000 HVGs. A nearest-neighbour graph (n_neighbors = 30) was computed between cells using these principal components, and PhenoGraph Leiden (v1.5.7)[56] clustering was applied on the principal component space (with k = 30). We established that clustering was robust to slight changes in k by reclustering the cells under varying k values and measuring consistency using the adjusted Rand index (sklearn package in Python, scikit-learn v1.4.2). Datasets were visualized with UMAP embeddings computed on the obtained principal component analysis.

Cell-type assignment. To assign cell-type labels, we manually assessed patterns of mean marker genes expression across clusters using custom marker genes[29] (Extended Data Fig. 2e,g and Supplementary Table 1). We also calculated DEGs for each cluster versus all other clusters with the scanpy.tl.rank_gene_groups() function in Scanpy using the Wilcoxon rank-sum test with Benjamini–Hochberg correction to identify the top expressed genes in clusters that were not easily identifiable. Once the neuronal cluster was identified, it was subsetted and reclustered using the first 30 principal components restricted to 2,100 HVGs. To identify excitatory cells in the ANT, expression of *Slc17A6* and *Slc1a1* was used[8]. To identify excitatory cells in the ACC, expression of *Slc17a7* and *Slc1a2* was used[8]. To identify inhibitory cells in both the ANT and ACC, expression of *Slc32a1* and *Slc6a9* was used[8]. A set of canonical marker genes for anterior or posterior thalamic nuclei were used in the ANT

samples and another set of marker genes to identify cortical layers was used in the ACC samples[29,57] (Supplementary Table 1).

Differential gene expression and Gene Ontology. Differential gene expression analysis between the HR and LR condition across time points was performed using the MAST R package[58] on log-normalized values. The MAST method fits a two-part generalized linear hurdle model, and includes a logistic regression to account for dropout events and a Gaussian model for continuous expression values. Reported *P* values were adjusted for multiple comparisons using the Benjamini–Hochberg method. DEGs were defined as having an adjusted $P < 0.05$ and log fold change ≥ 0.15 (Supplementary Table 3). GSEA was performed using the fast GSEA GSEApy implementation (v1.18.0; gseapy.gsea()) with default parameters. Gene Ontology enrichment was performed using the one-tailed hypergeometric test (over-representation analysis), with multiple comparisons correction. The GO_Biological_Function_2023 gene or the GO_Molecular_Function_2023 set libraries were used for Gene Ontology analysis[59].

Wasserstein distance computation. Global transcriptional distances between HR and LR samples across consecutive time points were estimated by calculating the Wasserstein distances using the Pertpy package (v0.9.3)[31] and the pt.tl.Distance("wasserstein") function using obsm_key = "X_pca". Transcriptional distances restricted to the DEGs were estimated using a custom code based on the Distance.bootstrap() Perpty function.

Abundance analysis. To visualize shifts in abundance between experimental conditions, cell densities per time point and condition were visualized on UMAP plots following a similar approach as previously reported[60].

Pseudotime analysis and visualization. To infer changes in cell states in the neuronal population from early-learning state throughout consolidation, we subsetted the ANT and ACC neurons and included clusters 0, 1, 4, 2 and 5 for the ANT and clusters 0, 1, 2, 3 and 7 for the ACC, as these clusters were the closest to each other on the UMAP space and probably represent more phenotypically similar states. We recalculated highly variable genes using the scanpy.pp.highly_variable_genes() function with the seurat_v3 method to obtain 1,000 HVGs. A nearest neighbour graph (n_neighbors = 30) was computed between cells using 30 principal components. We then applied pseudotime trajectory estimation. We chose to use the Palantir[32] (Palantir v1.0.0) algorithm, which assumes a known starting point and a unidirectional progression from a 'less-differentiated to a more-differentiated state' and hence orders cells along a continuum trajectory and assigns each cell a probability for reaching each terminal state. We then computed diffusion maps with Palantir (n_components = 5, n_waypoints = 500) to identify major axes of variation. Once the diffusion maps were computed, Palantir computes rescaled diffusion components on which the trajectory inference is performed. We selected a random starting cell from 'training day 2' for the ANT sample and from 'test day 2 HR' for the ACC sample. We also ran another trajectory analysis using CellRank (CellRank v2.0.6), with the transition matrix computed using the Cytotrace implementation[33]. Cytotrace assumes the number of genes expressed per cell as a signal of 'differentiation'. We observed that with both algorithms the 'terminal states' were not the latest sampled time points, suggesting that the extreme branches represented extreme phenotypes rather than terminal states.

In addition to computing pseudotime, Palantir also visualizes the data using tSNE on the multiscale diffusion components. We used this visualization to study shifts in population density along time points per condition (HR or LR). The density plots were made using the Python's Seaborn package (v0.13.1) and kdeplot() function. To estimate the percent of densities for neurons from each condition and time, we calculated the density of neurons in an embedding per condition using Scanpy's scanpy.tl.embedding_density() and visualized using scanpy.pl.embedding_density(). In a similar way, densities of Fos^+ neurons were also plotted on the trajectory tSNE embedding to observe shifts between samples. A neuron was defined as being Fos^+ if the expression of the *Fos* gene was greater than 0.1. To visualize genes correlated with the early-consolidation and late-consolidation branches and hence estimate fate probabilities, we used CellRank with the Palantir implementation and trajectory obtained previously with Palantir, using cr.kernels.PseudotimeKernel() with time_key='pseudotime_palantir'.

MiloR analysis. To quantify densities of HR versus LR neurons along the pseudotime trajectory and identify statistically significant enrichments, we used the MiloR (v3.21)[61] algorithm, which groups cells into partially overlapping local neighbourhoods and computes differential neighbourhood abundances across conditions (here HR versus LR). We constructed a *k*-nearest neighbour graph ($k = 30$) on principal components using the buildGraph() function and then constructed neighbourhoods on the *k*-nearest neighbour graph using the makeNhoods() function with default parameters (prop = 0.1, refined = true). The number of neurons present in each neighbourhood were quantified using the countCells() function and the statistical significance was assessed using testNhoods() and calcNhoodDistance() for spatial FDR correction. We visualized the distribution of log fold changes in each condition using the plotNhoodGraphDA() function with alpha set to 1 in all cases.

Gene target module estimation. To estimate the putative target genes of the identified transcriptional regulators, we used the Chea3 browser[62], which assembles transcription factor–target gene set libraries, and in this case, we used the Enrichr library. For each time point, we inputted the list of DEGs for the HR condition and identified the same transcriptional regulators derived from the pseudotime lineage correlation analysis. From the analysis, we obtained a list of overlapping genes predicting each transcriptional regulator.

Comparison of transcriptional regulator expression to public datasets. To compare expression levels of the identified ANT and ACC transcriptional regulators, we downloaded the corresponding prefrontal cortex and thalamus data sets from the Whole Mouse Brain Transcriptomic Cell Type Atlas[63], which were used in accordance with the Allen Institute for Brain Science Terms of Use. Pre-processing was carried out for the Mouse Brain Atlas data set in a similar manner as described earlier, and the ABC dataset version 10xv2-log2 was retrieved. Both datasets were clustered using Phenograph, and violin plots were obtained using the scanpy.pl.violin() function with default parameters.

Normality tests

To assess the distribution of our data, we performed normality and log-normality tests using GraphPad Prism (v9.5.1). For each dataset, normal quantile–quantile plots were generated to visually evaluate the fit to a Gaussian or log-normal distribution. Formal statistical tests for normality (Shapiro–Wilk) were also applied, as implemented in Prism. Quantile–quantile plots were used alongside *P* values from these tests to guide the choice of appropriate statistical analyses. Data failing both normal and log-normal tests were analysed using non-parametric methods.

Reporting summary

Further information on research design is available in the Nature Portfolio Reporting Summary linked to this article.

Data availability

Raw and processed scRNA-seq data from the mouse (accession GSE300871), raw and aligned ATAC-seq data (accession GSE304095),

and raw and aligned ChIP–seq data (accession GSE304099) are available from the Gene Expression Omnibus.

Code availability

No new algorithms were developed for this paper. The analysis code will be available on RajasethupathyLab GitHub.

50. Grandi, F. C., Modi, H., Kampman, L. & Corces, M. R. Chromatin accessibility profiling by ATAC-seq. *Nat. Protoc.* **17**, 1518–1552 (2022).
51. Hrvatin, S. et al. Single-cell analysis of experience-dependent transcriptomic states in the mouse visual cortex. *Nat. Neurosci.* **21**, 120–129 (2018).
52. Nott, A., Schlachetzki, J. C. M., Fixsen, B. R. & Glass, C. K. Nuclei isolation of multiple brain cell types for omics interrogation. *Nat. Protoc.* **16**, 1629–1646 (2021).
53. Azizi, E. et al. Single-cell map of diverse immune phenotypes in the breast tumor microenvironment. *Cell* **174**, 1293–1308.e36 (2018).
54. Wolf, F. A., Angerer, P. & Theis, F. J. SCANPY: large-scale single-cell gene expression data analysis. *Genome Biol.* **19**, 15 (2018).
55. Wolock, S. L., Lopez, R. & Klein, A. M. Scrublet: computational identification of cell doublets in single-cell transcriptomic data. *Cell Syst.* **8**, 281–291.e9 (2019).
56. Levine, J. H. et al. Data-driven phenotypic dissection of AML reveals progenitor-like cells that correlate with prognosis. *Cell* **162**, 184–197 (2015).
57. Phillips, J. W. et al. A repeated molecular architecture across thalamic pathways. *Nat. Neurosci.* **22**, 1925–1935 (2019).
58. Finak, G. et al. MAST: a flexible statistical framework for assessing transcriptional changes and characterizing heterogeneity in single-cell RNA sequencing data. *Genome Biol.* **16**, 278 (2015).
59. Fang, Z., Liu, X. & Peltz, G. GSEApy: a comprehensive package for performing gene set enrichment analysis in Python. *Bioinformatics* **39**, btac757 (2023).
60. Glasner, A. et al. Conserved transcriptional connectivity of regulatory T cells in the tumor microenvironment informs new combination cancer therapy strategies. *Nat. Immunol.* **24**, 1020–1035 (2023).
61. Dann, E., Henderson, N. C., Teichmann, S. A., Morgan, M. D. & Marioni, J. C. Differential abundance testing on single-cell data using *k*-nearest neighbor graphs. *Nat. Biotechnol.* **40**, 245–253 (2022).
62. Keenan, A. B. et al. ChEA3: transcription factor enrichment analysis by orthogonal omics integration. *Nucleic Acids Res.* **47**, W212–W224 (2019).
63. Yao, Z. et al. Whole mouse brain transcriptomic cell type atlas — 10x scRNAseq whole brain [dataset]. *NeMO* https://assets.nemoarchive.org/dat-qg7n1b0 (2023).

Acknowledgements We thank the Rockefeller Flow Cytometry Resource Center; R. Chaligné at the Single Cell Analytics Innovation Lab (SAIL) at the MSKCC for helping to optimize the sorting and sequencing of scRNA-seq samples; H. Tan in the laboratory of J. Friedman for generously providing Rosa26-LSL-spCas9-eGFP mice; Z. Gershon for troubleshooting single-cell dissociations; E. Azizi, O. V. Goldman and A. Sziraki for helpful discussions related to scRNA-seq analysis; N. Blobel and S. Nakandakari for assistance with in vitro CRISPR manipulations and sharing reagents; Y. Kishi for sharing the ATAC-seq protocol; and N. Heintz, E. Azizi and members of the Rajasethupathy laboratory for comments on the manuscript. This work is supported by a Kavli Pilot Grant (to A.T.), the NIH Medical Scientist Training Program T32GM152349 (to C.C.), a Cycle for Survival and an NCI grant P30 CA008748 (to the MSKCC Innovations Labs), funding from the Alan and Sandra Gerry Metastasis and Tumor Ecosystems Center (to SAIL, MSKCC), and grants from Irma T. Hirschl/Weill Caulier Trust, the Pershing Square Foundation, and the US National Institutes of Health under award numbers DP2AG058487 and RF1NS132047 (to P.R.). Figures 1a,d, 2a,b, 3a,d,h,k and 4a,g,i,j and Extended Data Figs. 8a and 9b were created using BioRender (https://biorender.com). All Allen Mouse Brain Atlas figures included in this work are adapted in accordance with the Allen Institute citation and rights policies, and used under their non-commercial open-access license.

Author contributions A.T., C.C. and P.R. conceived the study and designed the experiments. A.T. performed the optogenetic experiments, collected scRNA-seq samples with assistance from M.G. and developed the analysis pipeline for scRNA-seq. R.S. assisted with scRNA-seq analysis and pseudotime analysis. A.T. and C.C. developed a pipeline for in vitro and in vivo validation of sgRNAs, performed the in vivo CRISPR manipulations and conducted the behavioural testing. T.E. performed the photometry experiments and analysis. C.C. performed qPCR and immunohistochemistry or western blot validations. Y.H. collected samples for ATAC-seq. R.K. analysed the ATAC-seq data. C.C. collected samples for ChIP–seq. P.J.H. processed the samples. R.K. analysed the ChIP–seq data. A.T. performed the downstream analysis. A.T., C.C. and P.R. wrote the manuscript with input from all authors. P.R. supervised all aspects of the work.

Competing interests The authors declare no competing interests.

Additional information

Supplementary information The online version contains supplementary material available at https://doi.org/10.1038/s41586-025-09774-6.

Correspondence and requests for materials should be addressed to Priya Rajasethupathy.

Peer review information *Nature* thanks Jian Zhou and the other, anonymous, reviewer(s) for their contribution to the peer review of this work. Peer reviewer reports are available.

Reprints and permissions information is available at http://www.nature.com/reprints.

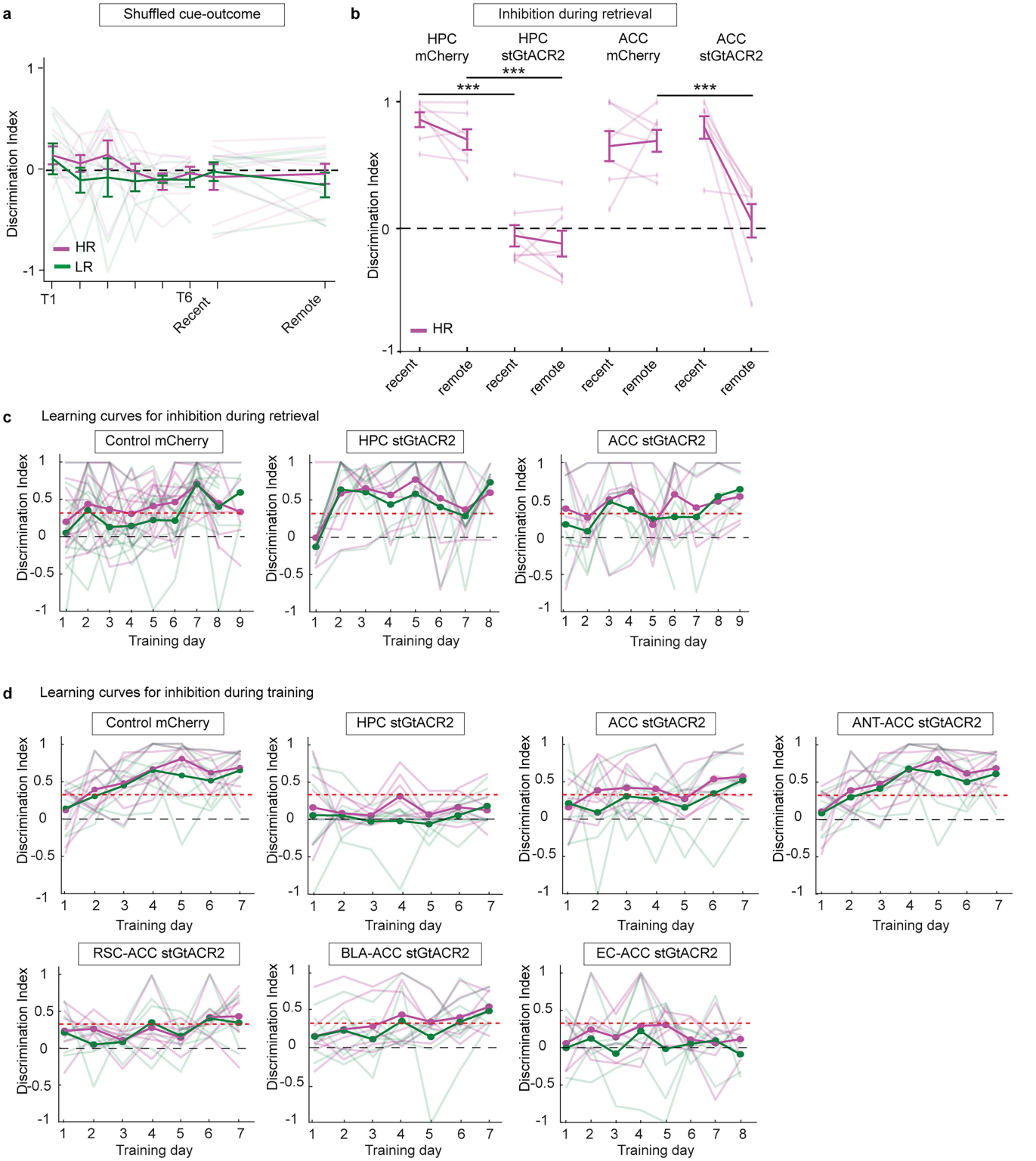

Extended Data Fig. 1 | Learning and retrieval performances during shuffled cue-outcome zones, inhibition during training and retrieval. a, Discrimination indices (DI) of learning and retrieval performance of mice exposed to shuffled cue-outcomes, $n = 8$ mice, DIs from individual mice shown (faded lines), with mean ± SEM (solid line). Dashed black line indicates DI = 0 (at chance). **b**, Optogenetic inhibition during recent and remote retrieval, $n = 7$ HPC mCherry control, $n = 8$ HPC stGtACR2 (inhibitory opsin), $n = 7$ ACC mCherry control, $n = 7$ ACC stGtACR2, individual animals shown (faded lines), with mean ± SEM (solid line). Light delivered during cue periods of each trial. Quantification of discrimination indices between HR and aversive lick rates, *** $P < 0.0001$ between HPC mCherry and HPC stGtACR2 at recent and remote retrieval, ***$P = 0.0001$ between ACC mCherry and ACC stGtACR2 at remote retrieval, One-way ANOVA with Bonferroni correction. **c**, Discrimination indices of learning performance in HR or LR for mice receiving inhibition during retrieval days, $n = 7$-8 mice per cohort, individual data points shown (faded lines), with mean ± SEM (solid line). Dashed red line represents learning criteria set as discrimination index ≥ 0.3. **d**, Discrimination indices of learning performance in HR or LR for mice receiving inhibition during training days, $n = 7$-9 mice per cohort, individual animals shown (faded lines), with mean ± SEM (solid line). ACC, anterior cingulate cortex. ANT, anteromedial thalamus. BLA, basolateral amygdala. EC, entorhinal cortex. HPC, hippocampus. HR, high repetition. LR, low repetition. rgCre, retrograde Cre. RSC, retrosplenial cortex. SSFO, stabilized step-function opsin. stGtACR2, soma-targeted Guillardia theta anion channelrhodopsin-2.

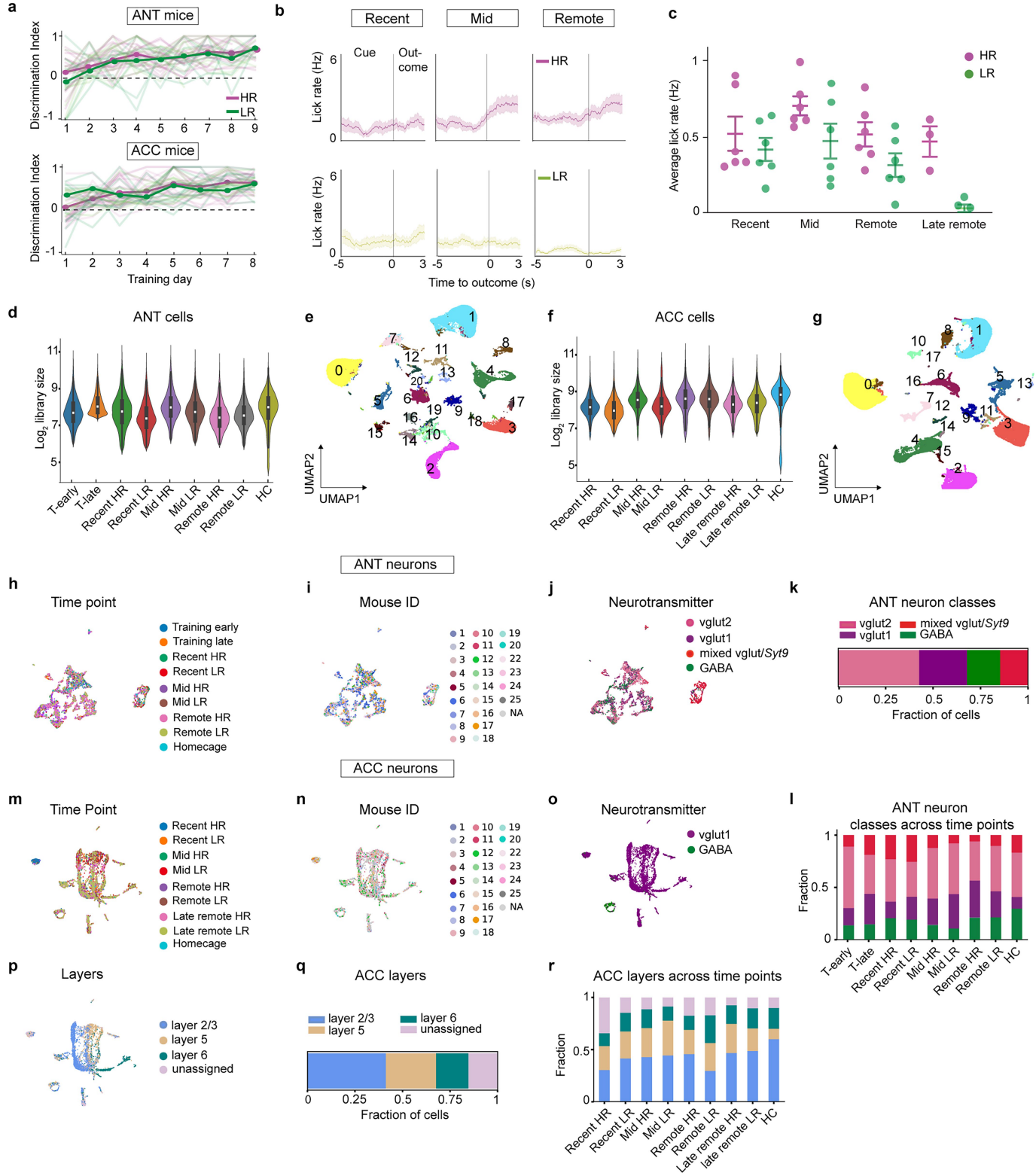

Extended Data Fig. 2 | See next page for caption.

Extended Data Fig. 2 | scRNA-sequencing behavioral data: cell typing and sub-setting of neurons. a, Discrimination indices of learning performance in HR and LR contexts of mice used for scRNA sequencing, *n* = 23 mice for ANT and 24 mice for ACC, individual animals shown (faded lines), with mean (solid line). **b**, Representative lick traces from one mouse showing trial averages of lick rate (Hz) in HR and LR at recent, mid and remote retrieval, data are mean (solid line) ± SEM (shaded area), *n* = 30-40 trials. **c**, Memory performance in HR and LR contexts of mice used for scRNA sequencing, *n* = 42 mice, data are mean ± SEM (error bars). **d**, **f**, Library size of ANT (d) or ACC (f) samples, *n* = 9 samples each region, median and interquartile range depicted (lower bound = 25th percentile, upper bound = 75th percentile, lower whisker = smallest data point ≥ (Q1 − 1.5 × IQR), upper whisker = largest data point ≤ (Q3 + 1.5 × IQR)). **e**, **g**, UMAP visualization of all cells from ANT (e) (*n* = 176566 cells) or ACC (g) (*n* = 145327 cells), clustered based on transcriptional profile and colored by cluster number. **h**, **m**, UMAP sub-clustering of cells identified as neurons in ANT (*n* = 5535 cells) (h) or ACC, (*n* = 5671 cells) (m) colored by time point. **i**, **n**, UMAP of ANT (i) or ACC (n) neurons colored by feature barcode of biological replicates. **j**, **o**, UMAP of ANT (j) or ACC (o) neurons colored by neurotransmitter class. **k**, Proportion of ANT neurons assigned to each neurotransmitter class. **l**, Breakdown of neuron classes across time points and conditions by proportion. **p**, UMAP of ACC neurons colored by cortical layer assignment. **q**, Proportion of ACC neurons assigned to each cortical layer. **r**, Breakdown of cortical layer assignment across time points and conditions by proportion. ACC, anterior cingulate cortex. ANT, anteromedial thalamus. HR, high repetition. LR, low repetition. T, training.

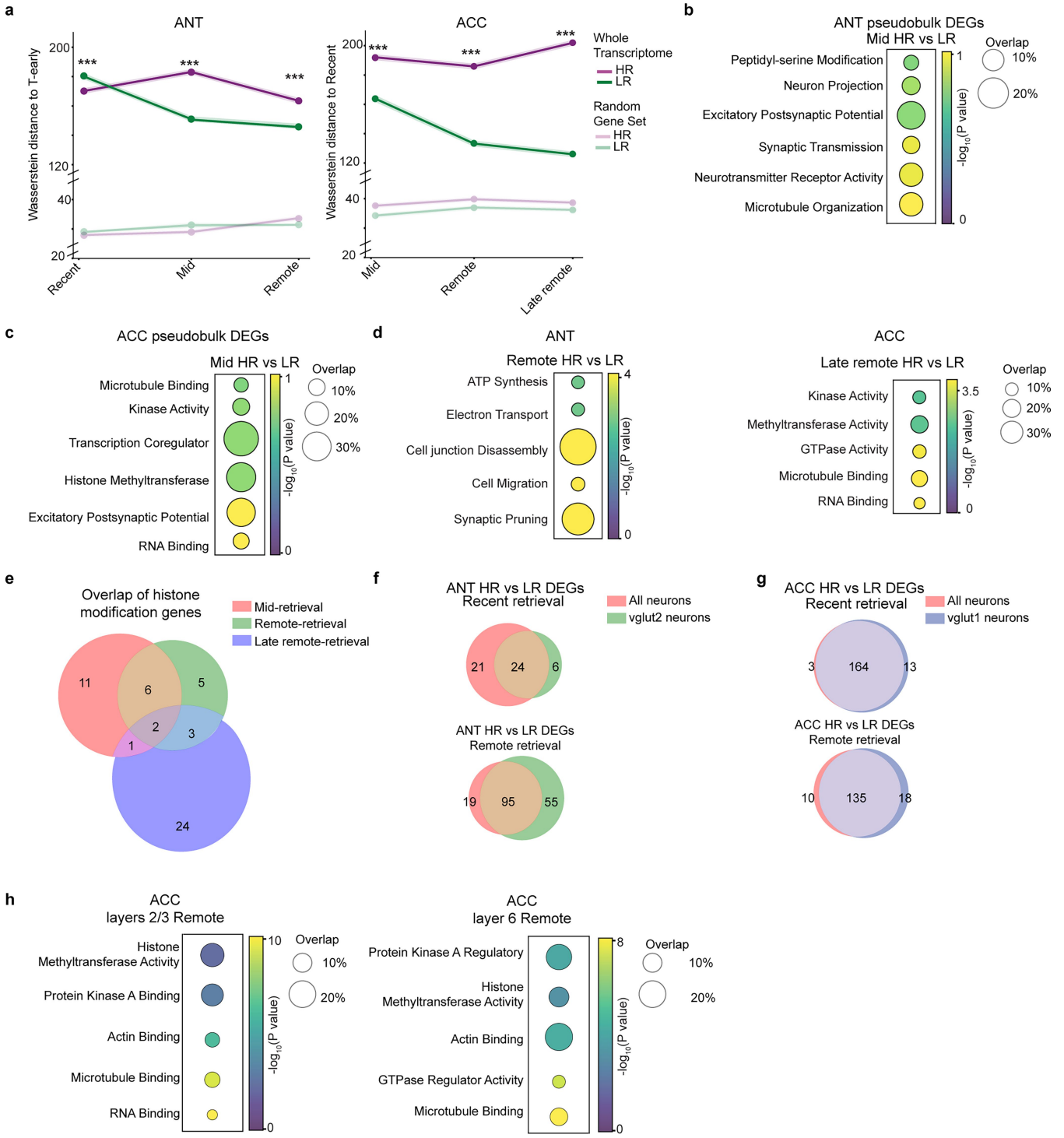

Extended Data Fig. 3 | ANT and ACC recruit distinct gene programs during memory persistence. a, Line plots of Wasserstein global transcriptional distance, using the whole transcriptome (solid colors) or a random set of genes (faded). Distances are to early-training in ANT (left) and to recent-retrieval in ACC (right), ***P < 0.0001 for global distances at recent, mid and remote retrieval HR vs LR in ANT, ***P < 0.0001 for global distances at mid, remote and late-remote retrieval HR vs LR in ACC, One-way ANOVA with Bonferroni correction. **b**, **c**, Gene ontology (GO) of ANT HR vs LR DEGs (b) or ACC HR vs LR DEGs (c) obtained using pseudo-bulk differential gene expression analysis. GO enrichment was performed using the one-tailed hypergeometric test (over-representation analysis), with multiple comparisons correction. Color gradient represents the nominal $-\log_{10}$(p-value), and circle size indicates percentage of genes within a GO term overlapping with total DEGs. **d**, GO analysis of genes upregulated in HR neurons at remote retrieval in ANT (left) and late-remote retrieval in ACC (right) using the same statistical parameters as (b), (c). **e**, Overlap of genes belonging to the histone methylation module across retrieval time points in ACC. **f**, Overlap between HR vs LR DEGs obtained using all ANT neurons, or *Vglut2* neurons, at recent and remote retrieval. **g**, Overlap between HR vs LR DEGs obtained using all ACC neurons, or *Vglut1* neurons, at recent and remote retrieval. **h**, GO analysis of DEGs from ACC neurons classified as cortical layer 2/3 or layer 6, using the same statistical parameters as (b), (c). ACC, anterior cingulate cortex. ANT, anteromedial thalamus. DEGs, differentially expressed genes. HR, high repetition. LR, low repetition.

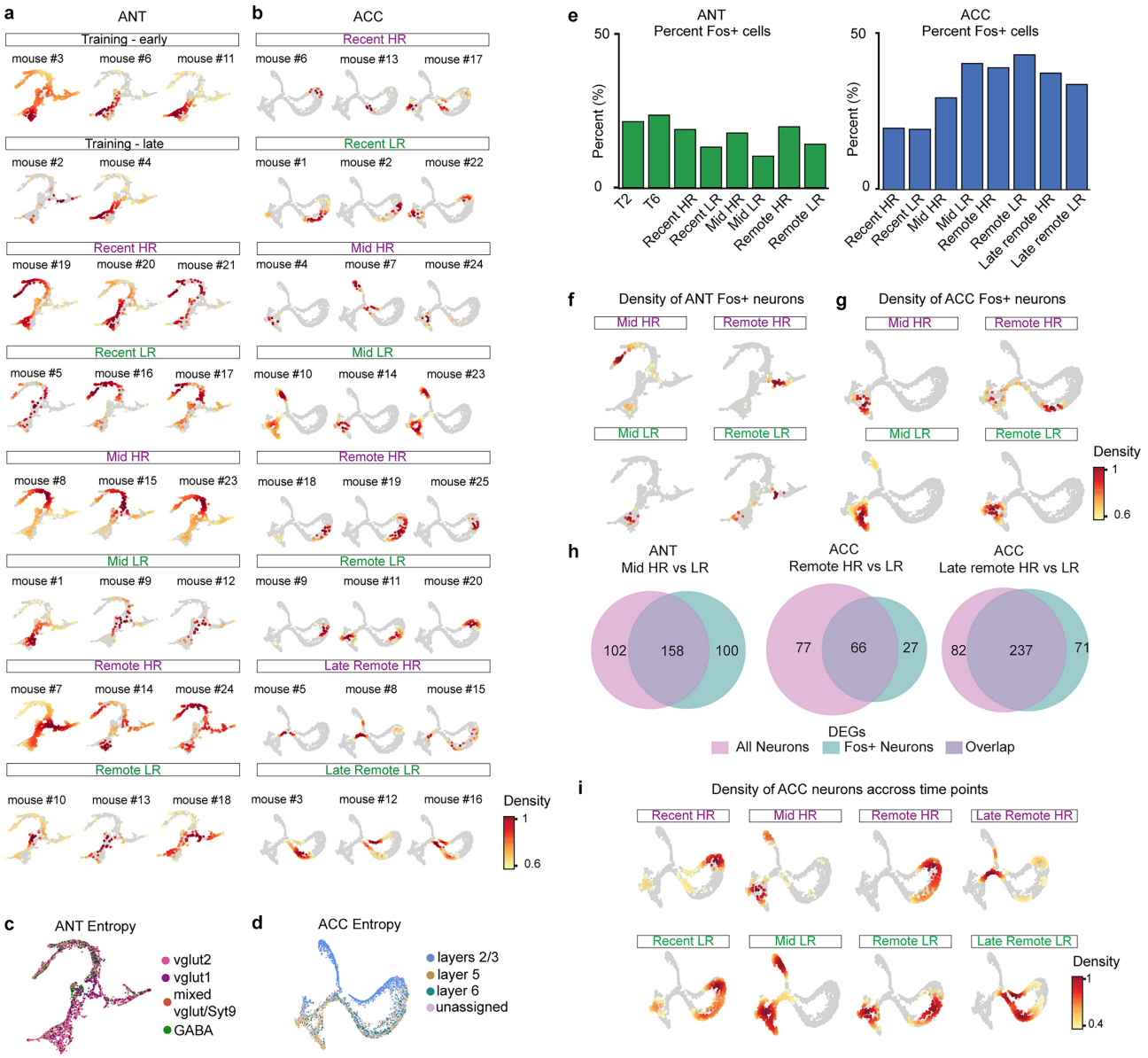

Extended Data Fig. 4 | Pseudotime trajectories capture macrostates associated with memory persistence. a, **b**, Kernel density estimate tSNE plots of ANT (a) or ACC (b) neurons for each biological replicate (n = 2-3 mice per time point) across all time points. **c**, **d**, tSNE visualization of ANT (c) or ACC (d) pseudo-time trajectory colored by neuronal class in ANT and anatomical layer in ACC. **e**, Bar plot of percent *Fos*+ neurons across time points in ANT (left) or ACC (right) neurons used to construct pseudotime trajectories. **f**, **g**, tSNE visualization of ANT (f) or ACC (g) trajectories, colored by *Fos*+ neurons with scored density >= 0.6. **h**, Overlap between DEGs obtained from either all neurons or only *Fos* + cells. Shown for mid-retrieval in ANT (left) and mid and remote retrieval in ACC (right). **i**, Density plots for HR and LR ACC neurons on the tSNE pseudotime space across retrieval days. ACC, anterior cingulate cortex. ANT, anteromedial thalamus. DEGs, differentially expressed genes. HR, high repetition. LR, low repetition.

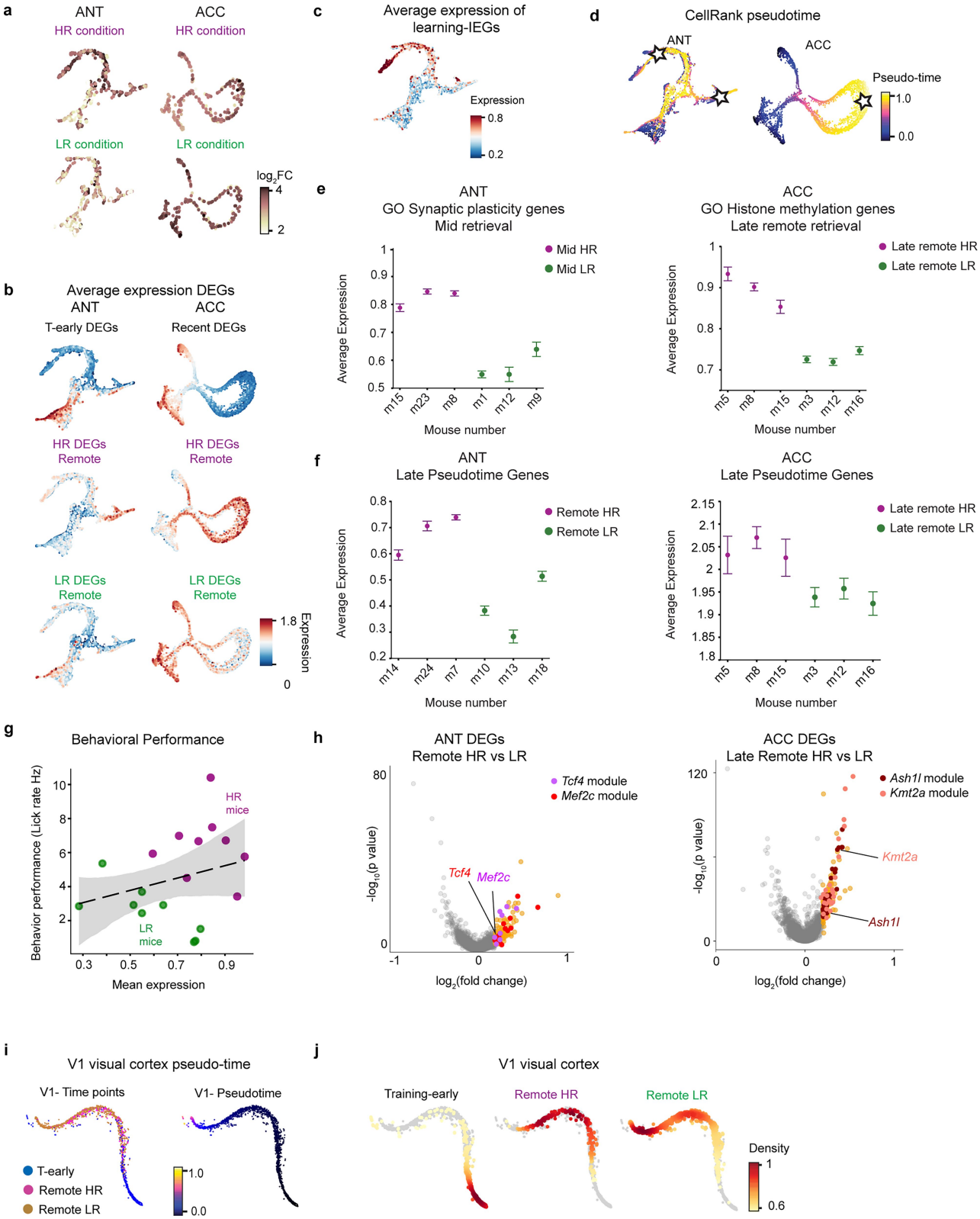

Extended Data Fig. 5 | See next page for caption.

Extended Data Fig. 5 | Expression of DEGs, GO modules and macrostate correlated genes along pseudotime trajectories. a, tSNE visualizations of ANT (left) and ACC (right) pseudotime trajectories, colored by neighborhood abundance of cells from HR or LR conditions. **b**, Pseudotime trajectories colored by average expression of DEGs from early-training and remote retrieval in ANT (left); recent-retrieval and late-remote retrieval in ACC (right), units are $\log_2$CPM + 1. **c**, ANT pseudotime trajectory colored by average expression of learning Immediate Early Genes (IEGs, units $\log_2$CPM + 1). **d**, Pseudotime trajectories of ANT (left) or ACC (right) obtained using the CellRank algorithm. Stars highlight apex points. **e**, Expression of genes associated with the synaptic plasticity GO module in ANT (left) at mid-retrieval, and the histone methylation GO module in ACC (right) at late-remote retrieval, each data point depicts an individual mouse, average expression represented in units $\log_2$CPM + 1, data are mean expression ± SEM (error bars). **f**, Expression of genes correlated with the late macrostate in ANT (left) or late-remote macrostate in ACC (right) across HR and LR, each data point depicts an individual mouse, data are mean ± SEM (error bars). **g**, Pearson correlation between behavioral performance during retrieval (measured as lick rate Hz) and average expression of genes shown in (e) and (f), each dot is a mouse. Mice tested on the HR condition in magenta and mice tested on the LR condition in green, r = 0.27. **h**, Volcano plots of DEGs between HR and LR at remote retrieval in ANT (left) or in ACC (right). Labeled genes indicate TRs, with TR modules highlighted by color. DEGs determined through a two-part generalized linear hurdle model, p-values adjusted for multiple comparisons using the Benjamini-Hochberg method. **i**, Left: pseudotime trajectory of V1 visual cortex neurons colored by time point. Right: V1 pseudo-time trajectory. **j**, Kernel density estimate tSNE plots of V1 visual cortex neurons across early-training, remote retrieval HR and remote retrieval LR. ACC, anterior cingulate cortex. ANT, anteromedial thalamus. DEGs, differentially expressed genes. HR, high repetition. LR, low repetition.

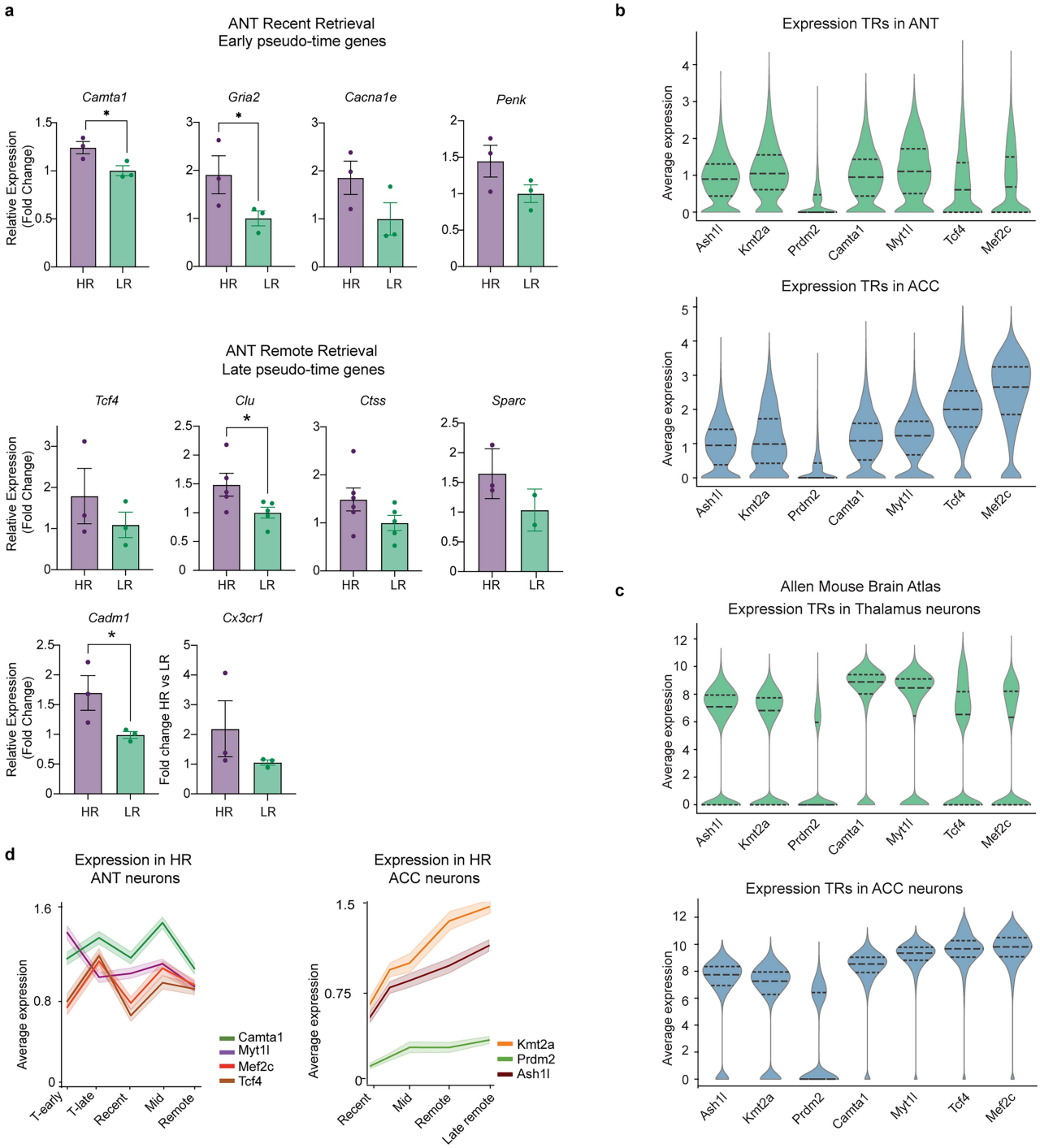

Extended Data Fig. 6 | Expression of transcriptional regulators' targets. **a**, Relative expression of pseudotime signature genes (assessed by qPCR) in ANT at early (top) and remote retrieval (bottom) between HR and LR mice, normalized to *Map2*. Data points represent biological replicates ($n = 3$ or $n = 6$), each corresponding to one animal and quantified as the mean of three technical replicates (Ct values), *P = 0.0211 for *Camta1*; *P = 0.0495 for *Gria2*; *P = 0.0286 for *Clu*, *P = 0.0384 for *Cadm1*, unpaired one-tailed Student's t-test, mean ± SEM shown. **b**, Average expression of all transcriptional regulators in ANT neurons ($n = 5535$ neurons, top) or ACC neurons ($n = 5671$ neurons, bottom) across conditions and time points (units $\log_2$CPM + 1), median and interquartile range depicted. **c**, Average expression of all transcriptional regulators in thalamus neurons ($n = 131212$ neurons, top) or ACC neuron ($n = 22385$ neurons, bottom) from the Allen Mouse Brain Atlas dataset (units $\log_2$ CPM + 1), median and interquartile range depicted. Reproduced from The Neuroscience Multi-Omic Archive under a Creative Commons licence CC BY 4.0. **d**, Line plots of average expression of ANT (left) and ACC (right) transcriptional regulators in HR neurons only across behavioral time points (mean ± SEM shown, units $\log_2$CPM + 1). ACC, anterior cingulate cortex. ANT, anteromedial thalamus. HR, high repetition. LR, low repetition.

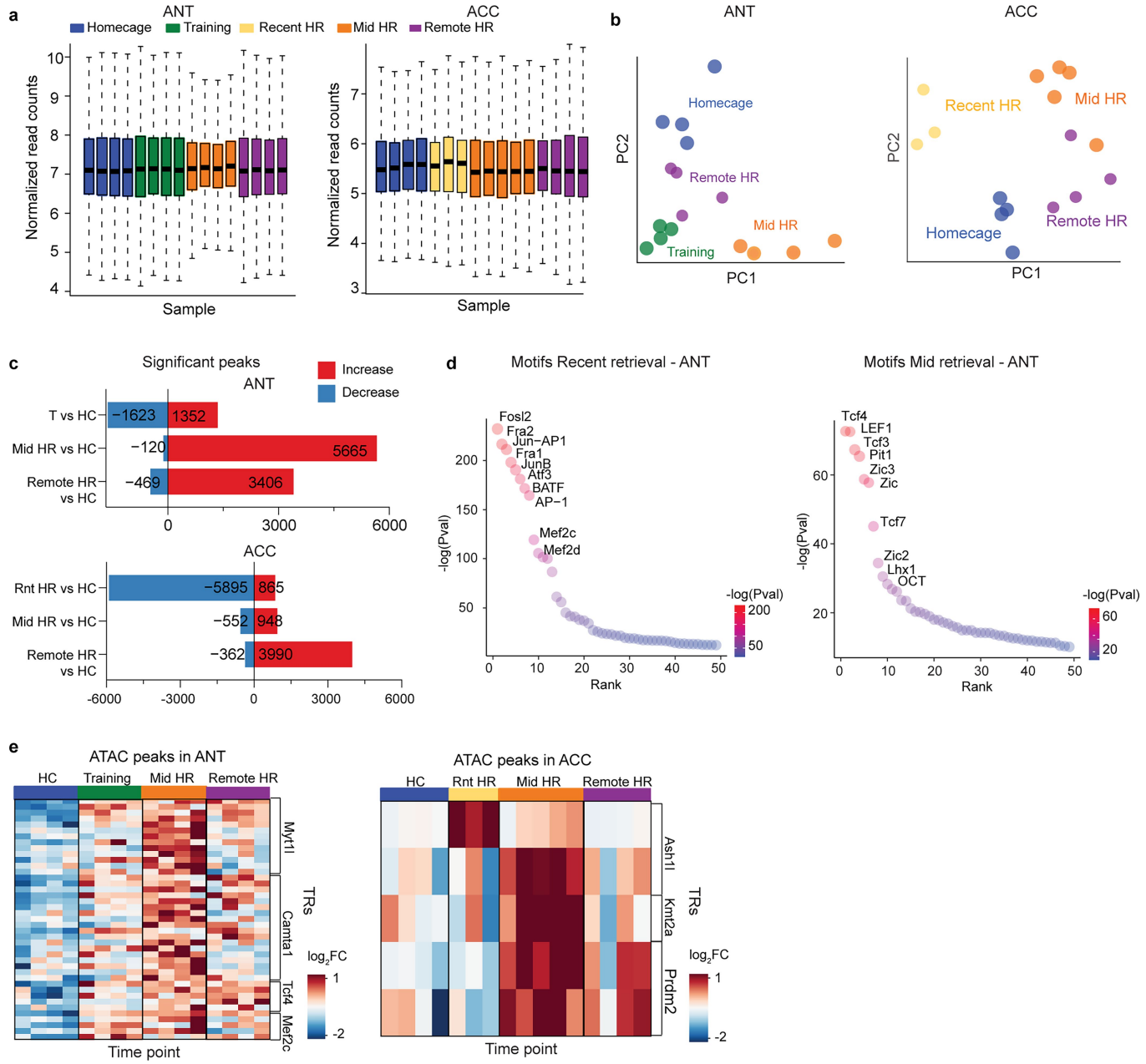

Extended Data Fig. 7 | ATAC peaks of ACC transcriptional regulators' modules remain accessible through remote retrieval. a, Boxplot of normalized read counts for ANT (left) and ACC (right) ATAC-seq samples, $n = 4$ mice per time point in ANT samples; $n = 3$ mice in recent retrieval, $n = 4$ mice in homecage and remote retrieval, $n = 5$ mice in mid retrieval in ACC samples. Median and interquartile range depicted (lower bound = 25th percentile, upper bound = 75th percentile, lower whisker = smallest data point ≥ (Q1 − 1.5 × IQR), upper whisker = largest data point ≤ (Q3 + 1.5 × IQR)). **b**, Principal component analysis (PCA) of samples from ANT (left) or ACC (right). Each point is an individual mouse, colored by the behavioral time point. **c**, Bar plot of significant peaks in HR condition versus home-cage (HC) comparisons across time points in ANT (top) or ACC (bottom) neurons. **d**, Sorted rank plot of transcription factor motifs for clustered peak modules at recent retrieval (left) or at mid retrieval (right) in ANT neurons, p-values for motifs are unadjusted and are derived from a one-sided binomial test against a nucleotide composition-matched background. **e**, Z-scored accessibility of ATAC peaks of ANT (left) or ACC (right) TRs, across time points. Columns are biological replicates (individual animals), n = 3-5 mice per time point, and rows are ATAC peaks. ACC, anterior cingulate cortex. ANT, anteromedial thalamus. HC, home cage. HR, high repetition. LR, low repetition. Rnt, recent. T, training.

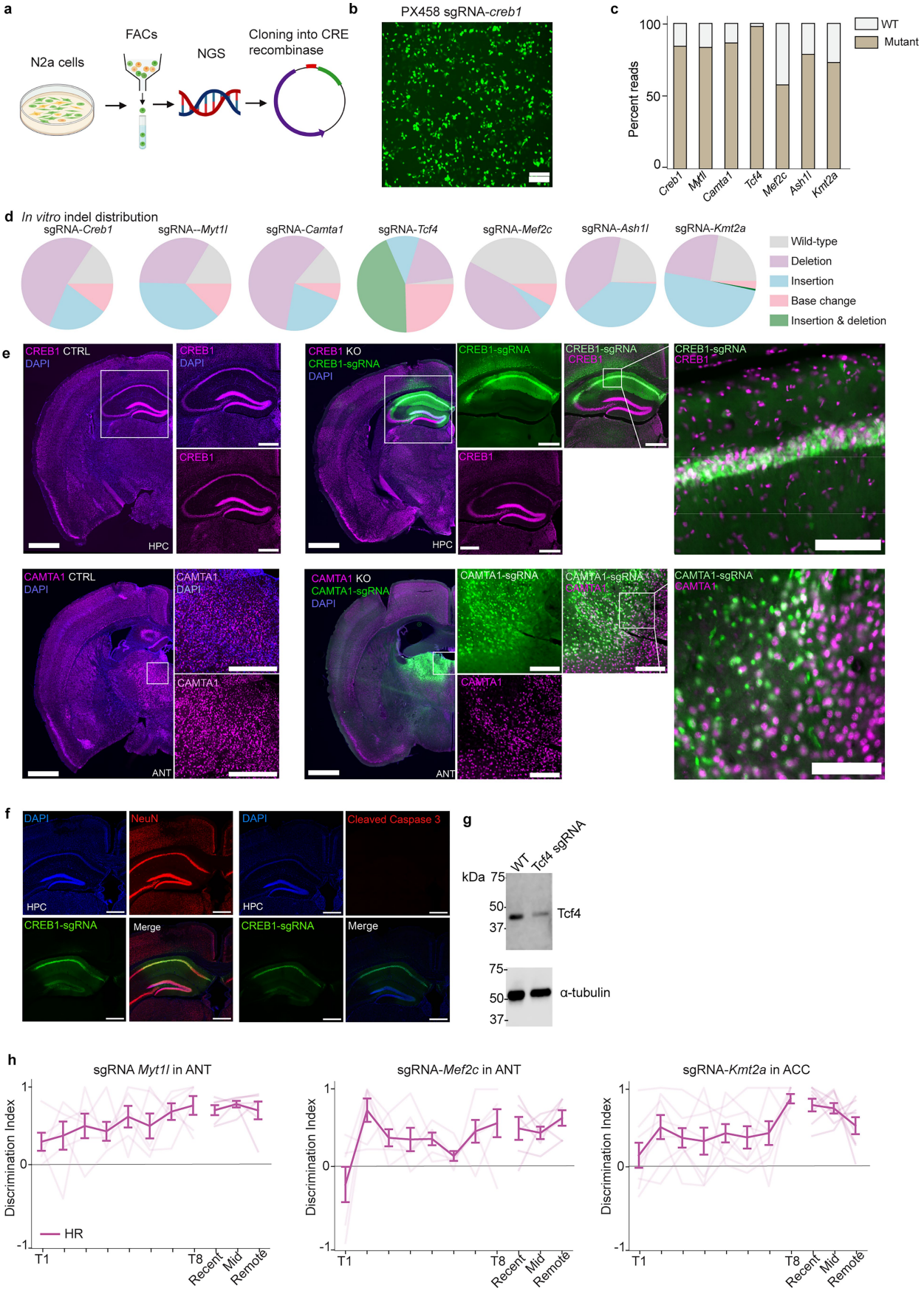

Extended Data Fig. 8 | See next page for caption.

Extended Data Fig. 8 | In vitro and in vivo sgRNA validation, and behavioral effects of TRs knockout. a, Schematic of in vitro CRISPR sgRNA screen. **b**, Neuro2A cells transfected with Px458-sgRNA-*Creb1-spCas9-GFP*, scale: 200 µm. Transfection efficacy was independently confirmed for each sgRNA by immunofluorescence, representative image shown. **c**, Percentage of WT vs mutant Sanger sequencing reads from genomic DNA isolated from Neuro2a cells transfected with Px458-sgRNA-*Cas9-GFP* after FACS sorting for GFP+ cells. For FACS gating strategy, see Supplementary Fig. 2c. *n* = 1 biological replicate per gene, showing the most efficient guide from the screen. **d**, Pie chart illustrating the breakdown of specific indel mutations identified by NGS of the PCR amplicon spanning the cut site from Neuro2a cells in (c) for select guides. **e**, Top left: coronal slice from a control *Rosa26-Cas9* knock-in mouse stained for Creb1 and DAPI in HPC. Bottom left: coronal slice from a control *Rosa26-Cas9* knock-in mouse stained for *Camta1* and DAPI in ANT. Scale bar = 1 mm in 4x, scale bar = 0.5 mm in 10x. Top right: coronal slice from a *Rosa26-Cas9* knock-in mouse injected with sgRNA-*Creb1-GFP* stained for Creb1 and DAPI in HPC, with inserts showing 10x and 40x field of view. Bottom right: coronal slice from a *Rosa26-Cas9* knock-in mouse injected with sgRNA-*Camta1-GFP* stained for Camta1 and DAPI in ANT, with inserts showing 10x and 40x field of view. Scale bar = 0.5 mm in 10x, scale bar = 0.1 mm in 40x. Representative images from one animal used in our behavioral experiments. **f**, Immunofluorescent staining of NeuN or Cleaved Caspase 3 in *Rosa26-Cas9* knock-in mouse injected with sgRNA-*Creb1-GFP* to evaluate extent of neuronal toxicity from AAV injection. Representative image shown from one mouse. Scale bar 0.5 mm in 10x. **g**, Western blot validation of *Tcf4*-KO from ANT tissue compared to control tissue, blotting performed on one animal (for uncropped blots, see Supplementary Fig. 1). **h**, Discrimination indices of learning and recall performances in HR of *Rosa26-Cas9* knock-in mice expressing sgRNA targeting *Myt1l, Mef2c or Kmt2a*. *n* = 6 sgRNA-*Myt1l* or sgRNA-*Mef2c*, *n* = 8 sgRNA-*Kmt2a* mice, individual data points shown (faded lines), with mean ± SEM (solid line). ACC, anterior cingulate cortex. ANT, anteromedial thalamus. KO, knockout. N2a, Neuro2a. WT, wildtype. The schematic in **a** was created using BioRender (https://biorender.com).

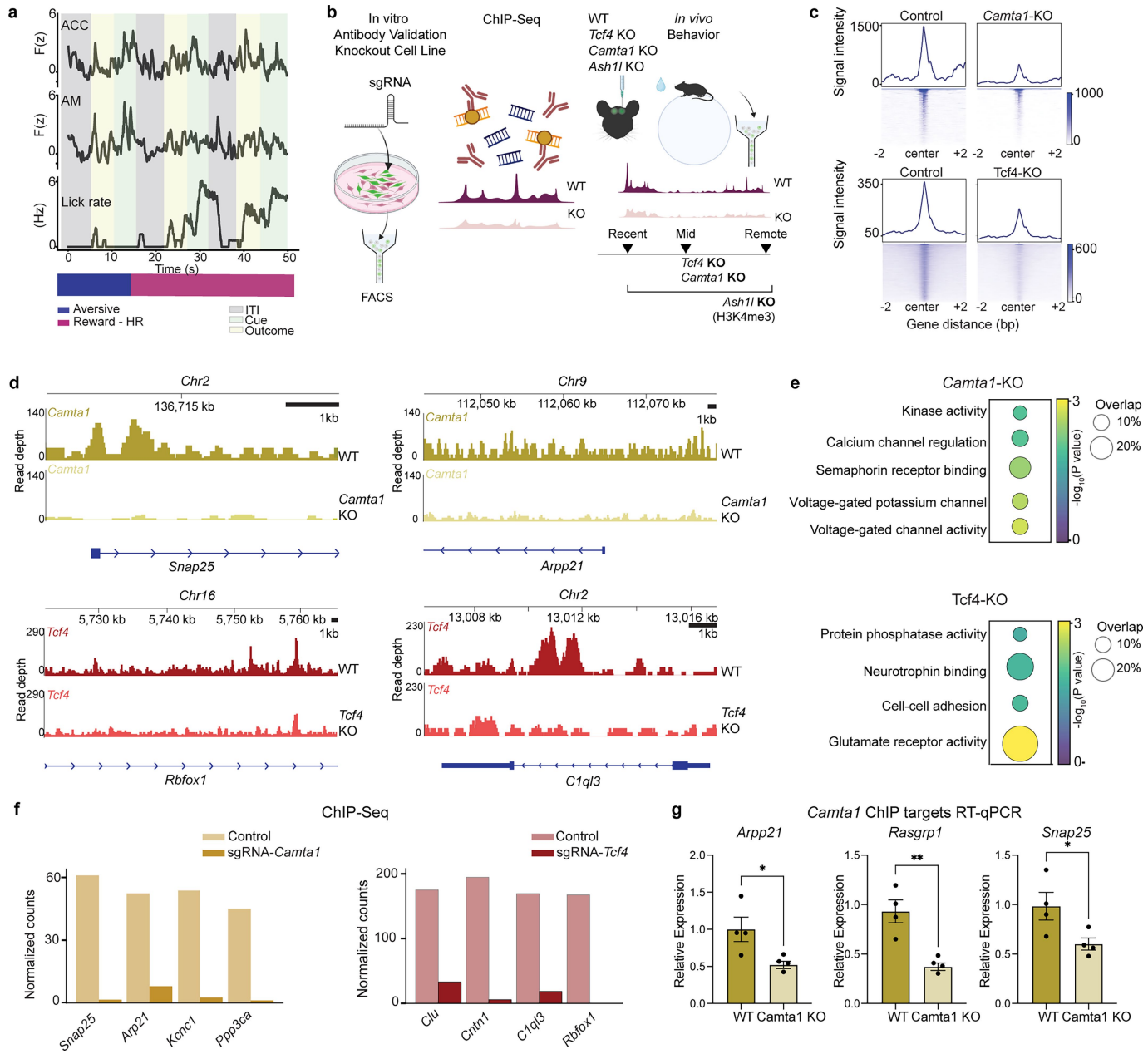

Extended Data Fig. 9 | Mechanistic analysis of identified TRs using photometry and ChIP-sequencing. a, Example traces of z-scored fluorescence intensity or F(z) from one control mouse from late training from ACC and ANT (AM) aligned to lick rate and task zones, three trials shown. **b**, Schematic of ChIP-sequencing workflow: selection and validation of antibodies via generation of knockout N2A cell lines, followed by ChIP-sequencing of samples collected at recent, mid and remote retrieval for WT and *Ash1l* KO (H3K4me3 antibody) or at mid-retrieval for WT and *Camta1/Tcf4* KO. Prior to ChIP-seq, dissected tissue was dissociated and FACS sorted for *NeuN*+ (WT controls) or *GFP*+ (KO) cells (For FACS gating strategy, refer to Supplementary Fig. 2e). **c**, Heatmaps of normalized ChIP-sequencing read densities centered at the midpoints (±2 kb) for WT controls, *Camta1* KO and *Tcf4* KO at mid retrieval. **d**, Top: *Camta1* ChIP-seq signal at *Snap25, Arpp21* gene loci for WT vs. *Camta1*-KO mice at mid retrieval. Bottom: *Tcf4* ChIP-seq signal at *Rbfox1, C1ql3* gene loci for WT vs. *Tcf4*-KO mice at mid retrieval. Tracks show normalized read density (RPKM) and are colored as darker shade for WT, lighter shade for KO. **e**, Gene ontology analysis of genes derived from ChIP-seq differential peak analysis of WT vs. *Camta1*-KO (top) or WT vs. *Tcf4*-KO (bottom) at mid retrieval, one-tailed hypergeometric test (over-representation analysis), with multiple comparisons correction. **f**, Left: bar plot of normalized counts in peak regions associated with *Camta1* target genes in control versus *Camta1* KO; $n = 1$ replicate sequenced for WT controls after pooling together NeuN+ sorted cells (neurons) from $n = 4$ animals; $n = 1$ sample sequenced for *Camta1* KO after pooling together GFP+ sorted cells (CRISPR/Cas9 edited) from $n = 9$ animals. Right: bar plot of normalized counts in peak regions associated with *Tcf4* target genes in control *versus Tcf4* KO, $n = 1$ sample sequenced, same number of animals used as for *Camta1*. **g**, qPCR validation of *Camta1* target gene expression in *Camta1*-KO mice. Bar graph showing the relative mRNA expression of plasticity-related genes (*Arp21, Rasgrp1*, and *Snap25*), previously validated by *Camta1* ChIP, in *Camta1*-KO) animals compared to WT controls. Expression levels are normalized to *Map2*. All animals used were run on VR behavior and dissected at the endpoint (Methods). Data are presented as mean ± SEM ($n = 4$ independent biological replicates/animals per cohort). *P = 0.00159 for *Arp21*; **P = 0.0018 for *Rasgrp1*; *P = 0.0231 for *Snap25*, unpaired one-tailed Student's t-test with Bonferroni-Dunn correction. AM/ANT, anteromedial thalamus, Chr, chromosome. F(z), z-scored fluorescence intensity, ITI, intertrial interval. KO, knockout. N2A, Neuro2a. WT, wildtype. The schematic in **a** was created using BioRender (https://biorender.com).

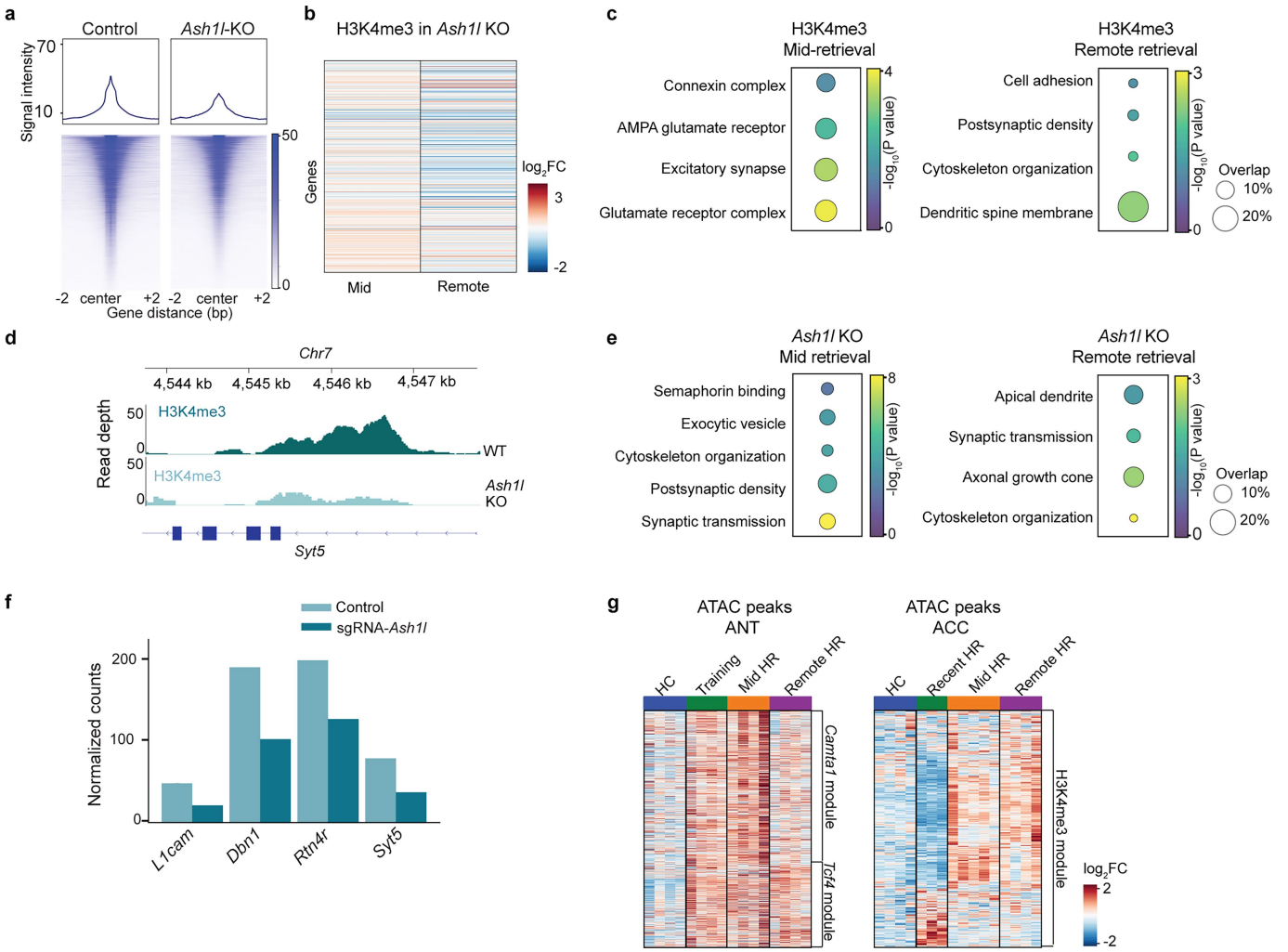

Extended Data Fig. 10 | Mechanistic analysis of identified TRs using ChIP-sequencing. a, Heatmaps of normalized H3K4me3 ChIP-sequencing read densities centered at the midpoints (±2 kb) for WT controls and *Ash1l* KO at mid retrieval. **b**, Heatmap of H3K4me3 marks in ACC *Ash1l* KO across mid and remote retrieval. **c**, Gene ontology analysis of genes associated with H3K4me3 peaks in WT controls at mid or remote retrieval, one-tailed hypergeometric test (over-representation analysis), with multiple comparisons correction. **d**, ChIP-sequencing signal at gene loci for H3K4me3 in WT or *Ash1l*-KO mice at remote retrieval. Tracks show normalized read density (RPKM) and are colored by condition (darker shade for WT, lighter shade for *Ash1l*-KO). **e**, Gene ontology analysis of genes associated with H3K4me3 peaks from *Ash1l*-KO mice at mid and remote retrieval, one-tailed hypergeometric test (over-representation analysis), with multiple comparisons correction. **f**, Bar plot of normalized counts in peak regions associated with *Ash1l* target genes in control versus *Ash1l*-KO samples, $n = 2$ independent biological replicates (each replicate is pooled dissected and GFP+ or NeuN+ FACS sorted tissue from 2 mice), mean of replicates depicted as bar. Every animal used underwent VR behavior and dissected at the endpoint (Methods). **g**, Left: Z-scored accessibility of ATAC peaks of *Camta1* and *Tcf4* modules derived from ChIP-sequencing in ANT neurons. Right: Z-scored accessibility of ATAC peaks of H3K4me3 module derived from ChIP-sequencing in ACC neurons. Columns are biological replicates, $n = 3$-5 mice per time point, and rows are ATAC peaks. Chr, chromosome. HC, home cage. HR, high repetition. KO, knockout. WT, wildtype.